Androgen receptor-negative prostate cancer is vulnerable to SWI/SNF-targeting degrader molecules

Phillip Thienger[1], Philip D. Rubin[1], Xiaosai Yao[2,3], Andrej Benjak[1], Sagar R. Shah[4], Alden King-Yung Leung[4], Simone de Brot[5], Alina Naveed[1], Minyi Shi[6], Julien Tremblay[3], Joanna Triscott[1], Giada Cassanmagnago[7], Marco Bolis[7,8,9], Lia Mela[1], Himisha Beltran[10], Yu Chen[11,12,13], Salvatore Piscuoglio[14,15], Haiyuan Yu[3], Charlotte K Y Ng[16,17], Robert L. Yauch[2§], Mark A. Rubin[1,17,18§*]

[1]Department for Biomedical Research, University of Bern, Bern, 3008, Switzerland.
[2]Department of Molecular Oncology, Genentech, South San Francisco, CA, USA.
[3]Department of Computational Sciences, Genentech, South San Francisco, CA, USA.
[4]Department of Molecular Biology and Genetics, Cornell University, Ithaca, NY, USA.
[5]COMPATH, Institute of Animal Pathology, University of Bern, Bern, Switzerland.
[6]Department of Proteomics, Lipidomics and Next Generation Sequencing, Genentech, South San Francisco, CA 94080.
[7]Computational Oncology Unit, Department of Oncology, Istituto di Ricerche Farmacologiche 'Mario Negri' IRCCS, Via Mario Negri 2, 20156 Milano, Italy.
[8]Institute of Oncology Research, Bioinformatics Core Unit, Bellinzona, TI 6500, Switzerland.
[9]Università Della Svizzera Italiana (USI), Faculty of Biomedical Sciences, Bellinzona, Switzerland.
[10]Department of Medical Oncology, Dana-Farber Cancer Institute, Boston, Massachusetts.
[11]Human Oncology and Pathogenesis Program, Memorial Sloan Kettering Cancer Center, New York, NY, USA.
[12]Weill Cornell Graduate School of Medical Sciences, Weill Cornell Medicine, New York, NY, 10065, USA.
[13]Department of Medicine, Memorial Sloan Kettering Cancer Center, New York, NY 10065, USA.
[14]IRCCS Humanitas Research Hospital, 20089 Rozzano, Milan, Italy.
[15]Department of Biomedicine, University Hospital Basel, University of Basel, 4001 Basel, Switzerland.
[16]SIB Swiss Institute of Bioinformatics, Lausanne, Switzerland.
[17]Bern Center for Precision Medicine, 3008, Bern, Switzerland.
[18]Inselspital, 3010, Bern, Switzerland.

§Co-senior authors
*Correspondence to: mark.rubin@unibe.ch (M.A.R)

Abstract

The switch/sucrose non-fermentable (SWI/SNF) chromatin remodeling complex is frequently deregulated during progression to castration-resistant prostate cancer (CRPC). Proteolysis targeting chimera (PROTAC) therapies degrading SWI/SNF ATPases offer a novel approach to interfere with androgen receptor (AR) signaling in AR-dependent CRPC (CRPC-AR). To explore the utility of SWI/SNF therapy beyond AR-sensitive CRPC, we investigated SWI/SNF ATPase targeting agents in AR-negative CRPC. SWI/SNF targeting PROTAC treatment of cell lines and organoid models reduced the viability of not only CRPC-AR but also WNT-signaling dependent AR-negative CRPC (CRPC-WNT), which accounts for about 10% of all clinical CRPC cases. In CRPC-WNT models, we discovered that SWI/SNF ATPase SMARCA4 depletion interfered with WNT signaling via the master transcriptional regulator TCF7L2 (TCF4). Functionally, TCF7L2 maintains proliferation via the MAPK signaling axis in this subtype of CRPC by forming a complex with β-Catenin and AP-1 transcription factor c-JUN. These data suggest a mechanistic rationale for MAPK inhibition or interventions that disrupt the formation of the pro-proliferative TCF7L2-β-Catenin-JUN complex in the CRPC-WNT subclass of advanced prostate cancer.

Introduction

Treatment-induced shifts in cancer cell identity, known as lineage plasticity (LP), lead to the emergence of tumors that may have little to no resemblance to the treatment-naïve tumors. The increased and earlier use of potent targeted cancer therapies are responsible for the emergence of aggressive, “plastic,” and untreatable cancers. In prostate cancer (PCa), LP can manifest when androgen receptor (AR)-driven adenocarcinoma (CRPC-AR) differentiates into AR-negative CRPC, which lacks both canonical AR signaling and neuroendocrine differentiation markers (double-negative CRPC) or acquires neuroendocrine features (CRPC-NE)[1-3]. Along with genomic alterations, epigenetic factors and induction of “stemness” (e.g., overexpression of SOX2) drive this process[4-7].

The epigenetic chromatin remodeling machinery complex switch/sucrose non-fermentable (SWI/SNF) orchestrates pluripotency and differentiation in embryonic stem cells[8], indicating its potential to maintain self-renewal in cancer and modulate lineage plasticity. In line with this, the SWI/SNF complex is mutated in over 20% of cancers[9]. However, in PCa, genomic alterations in the SWI/SNF complex are rare. Regardless, we and others have observed the dysregulation in SWI/SNF ATP-dependent helicases SMARCA2 (BRM) and SMARCA4 (BRG1) expression levels in mCRPC[7,10]. In non-small lung cancer (NSCLC), alterations in SWI/SNF ATPase expression (mainly loss of SMARCA4) have led to the discovery of a synthetic lethal relationship[11-13]. Moreover, recent studies nominated SMARCA2/4 as a regulator of key lineage factors in transcription factor-addicted cancers[14-16]. Also, other SWI/SNF complex subunits have emerged as therapeutic targets in multiple cancer types[17-19]. These findings led to the development of several inhibitors and proteolysis targeting chimera (PROTAC) degrader therapies against SWI/SNF complex subunits, including SMARCA2/4 and BRD9[12,20,21]. In CRPC-AR, degradation of the SWI/SNF catalytic ATPase subunits (SMARCA2, SMARCA4) compacts cis-regulatory elements bound by AR-associated transcription factors (TFs) that drive PCa proliferation[20].

Another critical pathway in cancer, especially during developmental processes, is the wingless and int-1 (WNT) pathway, which is partially regulated by the SWI/SNF complex[22-24]. Aberrations in WNT signaling are especially prominent in colorectal cancer but also emerge in other cancer types, such as CRPC[25-27]. This signaling pathway can be divided into the canonical (β-Catenin-dependent) and non-canonical (β-Catenin-independent) axis[28]. Canonical WNT signaling is regulated by the adenomatous polyposis coli (APC) factor, and its loss leads to overactive β-Catenin and its activators T-cell factor (TCF) and lymphoid enhancer-binding factor (LEF)[27,29,30]. In PCa, genetic changes in canonical WNT pathway genes are found in up to 22% of CRPC cases, but non-canonical WNT signaling is also altered in advanced PCa[31,32]. Further, the PCa stroma is known to secrete WNT proteins that activate WNT signaling in tumor cells to promote therapy resistance[33,34]. Recently, Tang et al. identified a subclass of CRPC, termed CRPC-WNT, that has traits of double-negative PCa (DNPC) but is enriched for mutations in WNT signaling pathway genes, accompanied by strong pathway activation through the TF TCF7L2, among others[35]. Interestingly, the factors that define the CRPC-WNT lineage are enriched for transcription factors that are hallmarks of lineage plasticity and identity (e.g., KLF5, TCF7L2, TCF7L1)[36-38].

In this study, we report that targeting SMARCA2/4 downregulates the lineage-defining WNT signaling signature[35] in CRPC-WNT patient-derived organoids. Mechanistically, this is accompanied by the formation of a complex chromatin-associated regulatory interactome consisting of AP-1 factors such as c-Jun and WNT factor β-Catenin, among others[39-42]. Interestingly, TCF7L2 was identified as the most active master transcriptional regulator in CRPC-WNT[35]. Indeed, we found that SMARCA4 depletion led to the eviction of TCF7L2 from AP-1 binding motifs and disruption of TCF7L2/β-Catenin interaction in CRPC-WNT. Knockdown of TCF7L2 and c-Jun dampened MAPK signaling, while MAPK inhibition decreased proliferation in CRPC-WNT. In summary, we found TCF7L2 to be a primary driver of CRPC-WNT, which is positively regulated by SMARCA4-dependent SWI/SNF activity to drive proliferative pathways, likely in concert with AP-1. This study strengthens the evidence that the SWI/SNF complex

plays a crucial role in advanced PCa and can be therapeutically exploited beyond AR-driven PCa adenocarcinoma.

Results

SMARCA2/4 is a vulnerability in DNPC patient-derived organoids (PDO)

In prior work, we discovered overexpression of SMARCA4 correlates with PCa progression, particularly neuroendocrine prostate cancer[7]**.** The testing of SMARCA2/4 targeting agents in PCa had been restricted to standard cell lines, covering only a limited representation of the commonly encountered genomic landscape and progression states seen in patients with CRPC. We posited that AR-negative CRPC may also manifest sensitivity to SWI/SNF ATPase inhibition. To address this, we used a novel PROTAC degrader, A947, that co-binds the SMARCA2/SMARCA4/PBRM1 bromodomains and the von Hippel-Lindau (VHL) ubiquitin ligase[12] (**Fig.1a**). This molecule has slight selectivity for SMARCA2 degradation, however at the concentrations used here it is equally potent for degradation of both ATPases within 1 hour in HEK293 cells (**Fig.1b**).

A947 was tested on a panel of PCa models, including established and organoid-derived cell lines and the non-neoplastic prostate line RWPE-1 (**Fig. 1c**). The four CRPC subclasses described by Tang et al.[35], AR-dependent (CRPC-AR) (n=6, quicksand), “WNT-driven” (CRPC-WNT) (n=4, orange), neuroendocrine prostate cancer (NEPC) (n=4, bordeaux), and “stem-cell-like” (CRPC-SCL, blue) (n=7) were treated for seven days with A947. We confirmed that AR-dependent cell models are particularly sensitive to SWI/SNF degradation[20]. In addition, we discovered that CRPC-WNT models were fully or partially responding to A947 (area under the curve (AUC<250)) (**Fig.1c, d**). Similar responses in “WNT-driven” PCa were observed with SMARCA2/4 PROTAC AU-15330 and inhibitor FHD-286, known to trigger cell death in AR-addicted PCa[20]. This was not the case with A858 epimer (SMARCA-binding control) or DMSO control (**Supplementary Fig. 1a**). The CRPC-WNT subclass shows features of DNPC based on the absence of NE and AR markers and sensitivity to fibroblast growth factor receptor inhibition (FGFRi)[1,2], indicating the clinical relevance of this subtype. Moreover, treatment with A947 with or without FGFRi led to more potent cell death in CRPC-WNT when compared with FGFRi combined with inactive epimer control A858 (**Supplementary Fig. 1b**).

SMARCA4 inhibition has been reported to be synthetic lethal with PTEN loss in PCa[43]. However, only two of the four CRPC-WNT models were PTEN deleted, indicating that the response to SMARCA4 degradation may be independent of its PTEN status[35]. CRPC-NE and CRPC-SCL organoids, as well as non-neoplastic prostate line RWPE-1, were not responsive to A947-treatment (**Fig. 1c**). Further, sensitivity to A947-treatment in CRPC-WNT could be phenocopied in a 3D spheroid proliferation assay and led to impaired spheroid morphology compared with A858 control (**Fig. 1e, f, Supplementary Fig. 1c**). To rule out potential off-target effects of A947 treatment, we used the most sensitive model, WCM1078, and treated it with increasing doses of VHL-ligand VL285 combined with a single dose of A947. Spheroid formation was increased with increasing doses of VL285, whereas spheroid formation was almost entirely impaired when VL285 was absent, while VL285 combined with DMSO did not affect spheroid formation (**Supplementary Fig. 1d**). Notably, levels of cleaved PARP1 (Asp214), Caspase-7 (Asp198), and Caspase-3 (Asp175) were increased in the CRPC-WNT lines, WCM1078 and MSK-PCa16 upon treatment with 1µM A947 indicating activation of the intrinsic pathway of cell death (**Supplementary Fig. 1e**).

To further characterize the changes induced by A947 treatment, we performed siRNA-mediated knockdown in all four CRPC-WNT models and one CRPC-NE model. All CRPC-WNT models responded strongly to SMARCA4 knockdown but only minimally responded to the knockdown of SMARCA2. CRPC-NE model WCM154, however, was unaffected by either knockdown (**Supplementary Fig. 2a, b)**. SMARCA4 containing SWI/SNF complex have been shown to associate with enhancers of lineage-defining genes, which could explain this selective dependency[20].

To rule out siRNA-mediated off-target effects, we elucidated the isolated effects of SMARCA4 depletion on cell growth using CRISPR-Cas9 sgSMARCA4 transduced organoids. We confirmed the cell-killing effect upon SMARCA4 knockdown using CRISPRi in all four CRPC-WNT lines by live cell analysis and/or

Celltiter Glo 2.0 (**Fig. 1g; Supplementary Fig. 2c, d**). Further, we checked SMARCA2/4 protein degradation levels over time in the four CRPC-WNT lines by immunoblot upon treatment with A947 (**Supplementary Fig. 2e**). The least sensitive model systems, MSK-PCa1 and MSK-PCa16, had higher baseline expression of SMARCA4 and maintained expression even after 48h of A947-treatment, which could explain decreased sensitivity to A947. In WCM1078 and WCM1262, SMARCA4 was completely degraded after 1h and 8h, respectively, after A947-treatment. Notably, the ubiquitin transfer pathway genes have been reported to be altered in PROTAC-resistant cells, leading to insufficient ubiquitinylation of PROTAC-targeted protein and impaired proteasomal degradation[44,45]. Indeed, we found that the A947-insensitive MSK-PCa1 model expressed lower protein levels of ubiquitin transfer pathway proteins VHL and Cullin-2 (CUL2), while intermediate A947-sensitive MSK-PCa16 had lower levels of VHL compared with A947-sensitive PDOs WCM1078 and WCM1262 (**Supplementary Fig. 2f**). When testing the SMARCA2/4 inhibitor BRM014, FHD-286, and PROTAC A947, we found that MSK-PCa1 was sensitive to BRM014 and FHD-286 but not to A947 (**Supplementary Fig. 2g**). Taken together, we posit that resistance or decreased sensitivity to PROTACs can emerge via modulations of the ubiquitin transfer pathway in PCa or differential baseline expression of the PROTAC target. Here, we show that small-molecule inhibitors can overcome this resistance.

CRPC-WNT is a clinically relevant subset of advanced CRPC

To determine how frequently the CRPC-WNT phenotype identified by Tang et al.[35] is seen clinically, we used publicly available single-cell sequencing (scRNA-seq) data from PCa cohorts (which include normal prostate/primary PCa (n=45), CRPC/NEPC (n=29) samples in total[2,46-50]). We found that the four signatures described by Tang et al.[35] could be identified in distinct clusters, especially the CRPC-WNT signature, which appeared in two distinct subclusters of CRPC separate from all other clusters (**Fig. 1h**). All remaining signatures, CRPC-AR, CRPC-NE, and CRPC-SCL, were more broadly distributed. Surprisingly, the CRPC-SCL signature was not only highly expressed in CRPC cases but also in normal and primary PCa (**Fig. 1h**). Overall, the signatures for CRPC-AR, CRPC-WNT, CRPC-NE, and CRPC-

SCL account for 38.3%, 11,7%, 22,9% and 22.4% of all CRPC cases, respectively. This underpins the clinical relevance of these signatures. These signatures could not characterize 4.7% of CRPC cases, indicating that additional rare phenotypes of CRPC may exist (**Fig. 1i**). These findings led us to investigate the underlying molecular mechanisms regulated by SMARCA4 in CRPC-WNT.

Lineage-defining programs are mitigated by SMARCA2/4 degradation in CRPC-WNT

To untangle the transcriptomic profile upon treatment with A947 and understand the heterogeneity of CRPC-WNT, we utilized single-cell RNA sequencing (scRNAseq) by SORT-seq[51]. WCM1078 and MSK-PCa16 were treated for 72h with 1µM A947 or control epimer A858. Single cells were sequenced at a depth of approx. 75K reads. A total of 1133 WCM1078 cells and 1183 MSK-PCa16 cells in the A858-treated condition and a total of 1184 WCM1078 cells and 997 MSK-PCa16 cells in the A947-treated condition were sufficiently sequenced. Both PDOs demonstrated homogenous profiles; the most prominent shift on the UMAP_1 dimension was induced by A947 treatment, resulting in another homogenous cluster (**Fig. 2a and e**). However, when checking for Tang et al. subclass defining signature scores[35], we found these to be heterogeneously expressed. We found that all CRPC signature scores were expressed as mutually exclusive in both PDOs, but the CRPC-WNT signature was most strongly expressed (**Supplementary Fig. 3a and b**). Notably, the CRPC-AR score was low and broadly distributed. The CRPC-WNT signature was most downregulated upon A947 treatment compared to any other CRPC score (**Fig. 2b, d, f, h**). The CRPC-SCL and CRPC-NE scores were also downregulated by A947 treatment compared with A858 treatment, but the positive clusters had low base levels compared with the CRPC-WNT positive cluster (**Supplementary Fig. 3a and b**). When comparing treatments, the weak CRPC-AR signature was either upregulated in WCM1078 or not significantly affected in MSK-PCa16.

When checking another signature for WNT signaling from colorectal cancer (CRC) (CRC WNT Score: "ASCL2", "NKD1", "RNF43", "CTNNB1", "WIF1", "SLC12A2", "OLFM4", "AXIN2", "LGR5") we found that

this signature overlapped with CRPC-WNT positive cells and that A947-treatment was sufficient to completely downregulate this score when compared with A858-treatment (**Fig. 2c, d, g, h**). The two Tang et al.[35] scores, CRPC-WNT and CRPC-SCL, were downregulated in bulk RNA-seq from A947-treated WCM1078 organoids (**Supplementary Fig. 4a**). Overall, several individual genes that define CRPC-WNT, as characterized by Tang et al.[35], were downregulated upon treatment with A947 in both organoid models (**Fig. 2i, j**).

By analyzing the pathway activity from scRNA-seq data using the single-cell regulatory network interference and clustering (SCENIC) tool, we observed a lowered activity of multiple TFs upon A947-treatment[52]. In both, WCM1078 and MSK-PCa16, activity of several TFs has been reduced; namely activity of FOX (e.g., FOXA1, FOXD1, FOXO6), TCF/WNT (TCF7L1, TCF7L2, TCF7, CTNNB1, LEF1), ETV (e.g., ETV4, ETV5) and AP-1 (e.g., JUN, JUND, FOSL1, ATF3) showed decreased activity (**Supplementary Fig. 3c, d**). In agreement, when checking the expression of the Top 25 highest-ranked transcription factors in CRPC-WNT, as determined by Tang et al.[35], in our bulk RNA-seq data from WCM1078, we found that KLF2, several TCF7 (TCF7L1, TCF7L2, TCF7), SOX (SOX13, SOX4), RUNX3 and LEF1 TFs were downregulated upon treatment with A947 (**Supplementary Fig. 4b**).

Further, we found by GSEA from bulk RNA-seq data in WCM1078 that after 24h and 48h treatment, multiple oncogene C6 signatures that are associated with mitogen-activated protein kinase (MAPK)-KRAS-MEK signaling are downregulated by A947-treatment (**Supplementary Fig. 4c, d**). This was also the case when overlapping 24h and 48h responses (**Supplementary Fig. 4e**). Interestingly, when checking for oncogene C6 signatures in WCM1078 scRNA-seq data, we found less clear downregulation of the bulk RNA-seq identified signatures while some MAPK signaling signatures were found (ERBB2_UP.V1_UP, MEK_UP.V1_UP) to be downregulated in the A947-treated condition (**Fig. 2k**). Moreover, we found that in MSK-PCa16 scRNA-seq the most downregulated C6 oncogene pathways were associated with WNT (LEF1_UP.V1_UP) and MAPK signatures (KRAS.600_UP.V1.UP,

KRAS.KIDNEY_UP.V1_UP) when treated with A947 (**Fig. 2l**). Both cell models had lower levels of the KRAS hallmark signature upon A947 treatment when compared with A858 in scRNA-seq data (**Fig. 2m, n**). Overall, overlap between WCM1078 A858 vs A947 data from bulk RNA-seq (48h), ATAC-seq (24h) and scRNA-seq (72h) revealed consistent downregulation of three signatures, namely MEK_UP.V1_UP, RAF_UP.V1_UP and RB_DN.V1_DN (**Supplementary Fig. 4e**). Interestingly, the downregulation of these proliferative signatures (e.g., MEK_UP.V1_UP) is relatively homogenous regardless of the underlying PCa lineage signatures, indicating the effect on proliferation might be a global secondary response to interference with lineage-defining programs (**Fig. 2o, p**). This data suggests a potential MAPK-associated proliferative axis that A947-treatment interferes with in CRPC-WNT, likely as an indirect effect upon the loss of the lineage-defining CRPC-WNT signature. To gain further insight into the epigenetic orchestration of this process, we examined the chromatin landscape in CRPC-WNT upon the treatment with A947.

CRPC-WNT is addicted to TCF7L2

The SWI/SNF complex mediates nucleosomal DNA packaging and is actively involved in regulating gene expression of multiple programs that can be crucial for cell survival. To mechanistically exploit changes in chromatin accessibility, we profiled the changes mediated by A947 treatment using the assay for transposase-accessible chromatin followed by sequencing (ATAC-seq). Within 24 hours, we found a near-complete loss at more than 7,000 sites in WCM1078 (CRPC-WNT), while only 160 sites were gained (**Fig.3a, Supplementary Fig. 5a**). Motif and binding analysis of A947-treatment compacted sites revealed binding motifs resembling WNT, FOX, and SOX motifs (**Fig. 3b**). FOX motifs are associated with the binding of FOXA1 and FOXM1, which are TFs that have been reported to be crucial mediators of PCa survival and translocation of β-Catenin[53,54]. TCF motifs are associated with TCF7, TCF3 (TCF7L1), and TCF7L2 binding sites, of which all are mediators of WNT signaling and CRPC-WNT[35]. Interestingly, TCF7L2 is the most active master TF in CRPC-WNT[35]. The treatment with A947 compared to A858 reduced TCF7L2 transcript levels in WCM1078 cells significantly after 24h (**Supplementary Fig.**

5b). Surprisingly, A947-treatment did not compact TCF7L2 promoter loci, indicating other mechanisms lead to the downregulation of TCF7L2 levels. Taken together, A947 treatment in WCM1078 led to closure at binding sites of multiple PCa-related TFs.

Since, TCF7L2 was identified as the most active TF in CRPC-WNT[35], we were particularly interested in understanding if CRPC-WNT cells are also dependent on TCF7L2. Thus, we tested the depletion of TCF7L2 in an additional CRPC-WNT organoid, MSK-PCa16, which has an amplification in TCF7L2, and found that siTCF7L2 decreased cell confluency (**Fig. 3c**). This phenotype was rescued by the transfection of a transient TCF7L2 rescue construct indicating the effect of siRNA on cell confluence is not due to off-target effects (**Fig. 3c**). In line with this, spheroid formation of WCM1262, WCM1078 and MSK-PCa1 was reduced when depleting TCF7L2 and β-Catenin (CTNNB1) using siRNA (**Fig. 3d, Supplementary Fig. 5c**). TCF7L2 was not expressed in CRPC-AR line LNCaP, and depletion of β-Catenin did not result in reduced confluence (**Supplementary Fig. 5d).** These data nominate TCF7L2 as a driver of the CRPC-WNT lineage.

It is important to consider that the organoid growth media contains R-spondin 1 (RSPO1), an activator of WNT-signaling. Therefore, we assessed the growth of WCM1078 and MSK-PCa16 in the absence of RSPO1 upon knockdown of β-Catenin and TCF7L2 to rule out artificial dependencies mediated by growth factor addiction in in vitro settings. The growth phenotype with and without RSPO1 showed no significant differences, and the absence of RSPO1 only marginally affected general growth rates of these PDOs (**Supplementary Fig. 5e**). Indeed, a recent study has identified that RSPO1 is not the inducing factor responsible for TCF7L2 expression in WNT-driven lineage progression[36]. This indicates that the WNT factors TCF7L2 and β-Catenin are potentially activated via non-canonical mechanisms or are constitutively active in CRPC-WNT.

Immunohistochemical staining of CRPC-WNT organoids treated with 1µM of control A858 or A947 for 24h revealed a strong downregulation of TCF7L2 signal (**Fig. 3e**). Further, reduced protein expression of TCF7L2 over time correlated with decreasing levels of SMARCA4 upon A947-treatment (**Fig. 3f**). Moreover, we tested if A947-treatment interfered with transactivation of TCF/LEF reporter plasmids in CRPC-WNT MSK-PCa16 grown in RSPO1-free media (**Fig. 3g**). Activation of TCFs by CHIR99021-mediated inhibition of GSK3β led to upregulation of luciferase signal from a transfected reporter plasmid driven by multimerized TCF-binding sites (TOPFlash)[55]. Interestingly, even without CHIR99021, the TOPFlash system was active when treated with A858, indicating that TCFs were constitutively active in MSK-PCa16. However, as stated previously, the relative luciferase signal could be further increased using CHIR99021. When treating the MSK-PCa16 with active PROTACs A947 and AU15330, the constitutive and induced relative TCF reporter signals could be drastically decreased by 92.5% and 89.7%, respectively. This is consistent with the downregulation of TCF7L2 over time (**Fig. 3e, f**). Interestingly, the relative TCF reporter signal was not completely reduced to the levels of the FOPFlash reporter. This could potentially be because not all TCF/LEF factors are affected by SMARCA2/4 PROTAC, leaving a residual activity signal (**Fig. 3g**). We did not find this constitutively activated TCF/LEF signal in HEK293T cells in which also the SMARCA2/4 PROTACS could not reduce the TOPFlash reporter signal (**Supplementary Fig. 5f**). This data suggests that TCF7L2 is indeed a lineage-defining master transcription regulator in CRPC-WNT specifically, which is regulated by SMARCA4-dependent SWI/SNF remodelers. Thus, we next aimed to determine the regulatory network of TCF7L2 in CRPC-WNT.

SWI/SNF ATPase degradation evicts TCF7L2 from AP-1 binding sites that are associated with proliferative signaling

To define the cistrome regulated by TCF7L2 in CRPC-WNT, we used chromatin immunoprecipitation followed by sequencing (ChIP-seq) analysis of WCM1078 organoids. In line with the chromatin closure at TCF7 motif sites by ATAC-seq, we found decreased TCF7L2 binding to chromatin in WCM1078

organoids upon exposure to A947 for 24h (**Fig. 4a**). A947 treatment led to the loss of 3,906 sites and a gain of only 54 sites compared with the A858 control. About 80% of lost regions are associated with distal regulatory regions commonly enriched for enhancers (**Fig. 4b**). Thus, we propose that in CRPC-WNT TCF7L2 has major intergenic regulatory functions, which are maintained by the SWI/SNF complex.

We performed HOMER motif analysis to answer the question of which chromatin sites are occupied by TCF7L2. This revealed that the loss of TCF7L2 ChIP signals were found at FOXA1, TCF3, and AP1-associated motifs (ATF3, AP2) upon treatment with A947 compared with A858 control (**Fig. 4c**). Gene-set enrichment analysis (GSEA) revealed enrichment of depleted peaks in regions associated with proliferative genes including previously identified MAPK associated pathways (EGFR_UP.V1_UP, RAF_UP.V1_DN, MEK_UP.V1_UP, ERBB2_UP.V1_UP) (**Fig. 4d**).

In agreement, downregulation of ERK (p44/42) phosphorylation at Threonine 202 and Tyrosine 204 was observed over time in A947-treated WCM1078 and MSK-PCa16 which correlated with increased cleaved-PARP (Asp214) levels (**Fig. 4e**). Surprisingly, the kinetics of the phospho-ERK downregulation did not follow the downregulation of SMARCA4 or TCF7L2. Thus, the decrease in MAPK genes may be due to direct effects on the chromatin/gene expression, as opposed to changes in the upstream protein cascade. The upstream MAPK cascade is potentially inhibited by decreased levels of downstream positive feedback activators, downregulated due to reduced chromatin accessibility at their gene loci upon A947 treatment.

In line with these findings, the inhibition of MAPK signaling by MEK1/2 inhibitors (MEKi) Trametinib and Cobimetinib decreased CRPC-WNT proliferation (**Fig. 4f**). CRPC-NE organoid WCM154 was also sensitive to MEKi but to a weaker extent than the CRPC-WNT organoids tested. Further, knockdown of TCF7L2 in CRPC-WNT cell lines decreased ERK phosphorylation, which was not the case in colorectal cancer cell line DLD-1 (**Supplementary Fig. 6a**).

These data prompted the question of how SMARCA4 maintains MAPK signaling. We observed that treatment of PCa cells with A947 resulted in the eviction of TCF7L2 binding from 80% of distal regulatory regions, which are often associated with enhancers (**Fig. 4b**). To understand the true nature of these distal regulatory regions sites affected in CRPC-WNT when treated with A947 we performed enhancer RNA (eRNA) sequencing using PRO-cap.

TCF7L2-occupied AP-1 enhancer sites are inactivated upon degradation of SMARCA2/4

One of the earliest events in gene transcription is the activation of distal cis-regulatory enhancer regions and its associated transcription of eRNA. Since changes in chromatin architecture are extremely rapid upon impairment of the SWI/SNF complex, it is not surprising to see the loss of accessibility of distal regulatory regions upon SWI/SNF complex inactivation[56,57]. We showed that 80% of lost chromatin regions occupied by TCF7L2 are distal regulatory regions from which TCF7L2 is evicted by A947-treatment (**Fig. 4b**). Thus, we explored the impact of A947-treatment on eRNA expression using the nuclear run-on followed by cap-selection assay (PRO-cap), which is the most sensitive method to identify active enhancers by measurement of endogenous eRNA transcription levels genome-wide at base-pair resolution[58] (**Fig. 5a**). Active enhancers loci are precisely delineated by detecting active transcription start sites that are dependent on the associated core promoter sequences[59]. When treating WCM1078 spheroids for 24 with either A858 or A947 followed by GRO/PRO-cap, we found 1069 of eRNAs aka distal peaks (+/- 1kb) to be downregulated (blue) while only 2 distal peaks were upregulated (red) by A947-treatment (**Fig. 5b**). Overall correlation with our ATAC-seq data was moderate ($R=0.59$, $p<0.001$), indicating the potential discovery of additional cis-regulatory sites via PRO-cap (**Supplementary Fig. 6b**). Indeed, it has been shown that not all open chromatin regions contain active eRNA transcription by Pol II[59]. Interestingly, the correlation between PRO-cap and the TCF7L2 ChIP-seq was greater ($R=0.67$, $p<0.001$) than with ATAC-seq (**Supplementary Fig. 6c**).

Next, we used the genomic search engine GIGGLE to identify and rank genomic loci shared between publicly available genome interval files[60]. We determined the GIGGLE score to be enriched for transcription factors associated with AP-1 (JUND, FOS, FOSL2, JUN), as well as FOXA1, ETV5, and TCF7L2 among the top 20 repressed distal peaks (**Fig. 5c**). HOMER motif analysis confirmed most enriched motif in depleted distal peak in AP-1 (**Fig. 5d**). Due to the good correlation between our TCF7L2 ChIP-seq and our PRO-cap distal peak data, as well as the fact that we found AP-1 motifs among the top enriched motifs in depleted peaks, we overlapped these two data sets. We found that these TCF7L2-occupied sites are enriched in the PRO-cap regions in the A858-treated condition but lost in the A947-treated condition (**Supplementary Fig. 6d**). These findings indicate that the AP-1 cistrome is primarily affected by A947 treatment in CRPC-WNT.

Since c-JUN is known to form a pro-proliferative complex with TCF7L2 and β-Catenin in colorectal cancer [36], we were also interested if such a complex is formed in CRPC-WNT. Indeed, in vitro siRNA-mediated knockdown of JUN in CRPC-WNT lines WCM1078 and MSK-PCa16 led to decreased confluence (**Fig. 5e**). In addition, siJUN led to reduced phosphorylation of ERK (p44/42) at Threonine 202 and Tyrosine 204 (**Supplementary Fig. 6e**). Further, c-Jun protein levels were downregulated upon treatment with A947 in WCM1078 and MSK-PCa16 (**Fig. 5f**). To prove that JUN interacts with TCF7L2 and β-Catenin, we performed a proximity ligation assay (PLA) using a β-Catenin antibody combined with an antibody against TCF7L2 or phosphor-c-Jun (Ser73) (**Fig. 5g, Supplementary Fig. 6f**). In the presence of the control A858, we detected a strong PLA signal (red) between β-Catenin and TCF7L2 or phospho-c-Jun, which was absent in the presence of A947 in both CRPC-WNT lines MSK-PCa16 and WCM1078. This was confirmed by co-immunoprecipitation of β-Catenin in MSK-PCa16 (**Supplementary Fig. 6g**). Indeed, we found that β-Catenin binds TCF7L2 and c-Jun. The interaction between β-Catenin with TCF7L2 and c-Jun was decreased upon A947-treatment compared with A858 treatment (**Supplementary Fig. 6g**). To summarize, we postulate that CRPC-WNT utilizes WNT and AP-1 TFs to bind enhancers and promoters of pro-proliferative genes. SMARCA4-containing SWI/SNF complexes

maintain accessibility to these chromatin regions, and the disruption of this chromatin remodeler leads to the blockage of assembling a WNT/AP-1 complex on the chromatin.

Discussion

The standard approach to treating advanced prostate cancer has been to modulate the AR axis either through direct or indirect means[61]. Drugs such as enzalutamide or abiraterone are potent ARSi used clinically, and other agents, including AR-degraders, are in clinical development. Resistance to ARSi therapy manifests in manifold ways (e.g., *AR* gene mutation, amplification, enhancer amplification), as well as a subset acquiring epigenetic rewiring towards AR-negative phenotypes[10].

As mentioned, AR-negative PCa had previously been classified as CRPC-NE or DNPC. CRPC-NE is characterized by a small-cell morphology, stemness, and the expression of neuronal and NE marker genes; however, while DPNC is also AR-negative, it shows no evidence of neuroendocrine differentiation based on morphology or expression of classical NE markers[1,62]. From this classification emerged two novel subtypes that branch into the DNPC category: CRPC-WNT and CRPC-SCL[35]. Tang et al. suggested that CRPC-WNT is TCF/LEF TF driven, while CRPC-SCL is YAP/TAZ TF dependent. Unfortunately, targeting these specific pathways directly remains a clinical challenge[63,64]. An alternative approach is to interrupt master transcriptional lineage programs by targeting TF cofactors and associated epigenetic regulators. Among these epigenetic regulators is the chromatin remodeler SWI/SNF complex, which we have previously found to be dysregulated in PCa throughout disease progression and thus represents a viable therapeutic target in early but also late-stage disease[7]. The SWI/SNF complex has been linked to being a predominant orchestrator of lineage-defining transcriptional programs, especially in master TF-addicted cancers[16].

A recent study in AR-dependent PCa found that PROTAC degraders that target the SWI/SNF complex disrupt the enhancer and promoter looping interaction that wire supra-physiological expression of lineage-driving oncogenes, including the AR, FOXA1, and MYC[20]. However, the number of AR-negative models tested in this study were limited; therefore, we examined the effect of SWI/SNF ATPase PROTAC

degraders in a PCa-focused screen. We utilized both AR-dependent and a broad spectrum of AR-negative PCa model systems, including CRPC-NE, CRPC-WNT, and CRPC-SCL. Here, we report that VHL-dependent degraders for SWI/SNF ATPase components decrease proliferation and spheroid formation in organoids of the CRPC-WNT phenotype for which no standard-of-care treatment exists. Clinically, CRPC-WNT tumors account for around 10-11% of all CRPC cases (**Fig. 1h**)[12,20,35]. We found that the SWI/SNF ATPase SMARCA4, but not SMARCA2, depends on the CRPC-WNT phenotype. Transcriptional analysis on the single-cell level of CRPC-WNT organoids revealed a certain degree of heterogeneity within these organoids; more specifically, we found variable expression of the signature scores for CRPC-NE, CRPC-WNT, and CRPC-SCL. However, the fraction of the CRPC-NE and CRPC-SCL signature-positive cells compared with CRPC-WNT was drastically lower in these organoids. This aligns with the fact that PCa is a highly heterogeneous disease and could potentially explain that not all CRPC-WNT organoids fully respond to A947 treatment (e.g., MSK-PCa16)[65].

Mechanistically, we identified a complex network orchestrated by WNT-signaling factor TCF7L2, the most active TF in CRPC-WNT[35]**,** to be attenuated upon degradation of SMARCA2/4. We show that TCF binding sites, specifically TCF7L2 sites, were compacted when SMARCA4 was absent. TCF7L2 itself was downregulated following treatment of WCM1078 and MSK-PCa16 cells with A947, and TCF7L2 depletion resulted in selective cell killing of CRPC-WNT models, but no other WNT-driven cancers were affected. This indicates that TCF7L2 is involved in maintaining a niche of DNPC but potentially via non-canonical, “nontraditional” WNT signaling. In line with this, we discovered that TCF7L2 binds AP-1 DNA elements and that TCF7L2 is evicted from these elements following the inhibition of the SWI/SNF complex. This indicates that TCF7L2 potentially gets hijacked from its traditional role in canonical WNT signaling to assist in driving AP-1 transcriptional circuits.

AP-1 is associated with several proliferative pathways, including the MAPK signaling pathway[66,67]. Interestingly, we found these proliferative pathways to be enriched in downregulated gene-set signatures

in our sequencing data. Further, MEK1/2 inhibition in CRPC-WNT led to potent cell death. This is underpinned by the finding that MAPK signaling is a dependency in DNPC and that clinical trials with Trametinib in CRPC have entered Phase II (**NCT02881242**)[1,68]. However, these trials were not biomarker-based and were conducted in patients who progressed after AR-targeted therapy. Thus, based on our data, it may be beneficial to clinically assess the utility of TCF7L2 as a biomarker in CRPC to predict response to SMARCA4 or MAPK targeting therapies.

Globally, AP-1 enhancer sites were most affected when the SWI/SNF complex was interfered with in CRPC-WNT. Indeed, SWI/SNF activity is needed to retain enhancers in an open conformation, as demonstrated by recent studies[56,57]. These findings are complemented by the finding that the deregulation of multiple transcription factor pathways is indeed contributing to the epigenetic bases of CRPC, including EGFR/ERBB (MAPK), TCF7L2/β-Catenin (WNT), and JUN/FOS (AP-1)[69]. Several studies show that TCF7L2/β-Catenin directly interacts and signals in concert with AP-1 in different cancer malignancies to promote disease progression[39,40,42]. Similarly, we have found that SWI/SNF complex degradation leads to the disruption of the TCF7L2/β-Catenin/AP-1 complex in CRPC-WNT.

In summary, we nominated the SWI/SNF chromatin remodeling complex, primarily SMARCA4, as a vulnerability in WNT-dependent DNPC. Thus, we propose a model in CRPC-WNT in which canonical WNT signaling components are hijacked to interact with AP-1 factors to bind AP-1 binding sites that regulate pro-proliferative genes, of which some activate the MAPK signaling axis. We postulate that c-Jun tethers the TCF7L2/β-Catenin complex to these specific AP-1 motifs and thus functions as an interface for this heterodimer. Impaired maintenance of chromatin accessibility by SMARCA4-containing SWI/SNF complexes potentially blocks the assembly of this “driver” complex on the chromatin (**Fig. 6**). Paralleling other studies in CRPC and SCLC, our data suggests that SWI/SNF-targeting agents have general efficacy in cancers that are strongly driven by nuanced master transcriptional regulators[14,20]. Further, we posit that FGFR inhibition could be another viable approach to target CRPC-WNT cancers

and anticipate a mechanistic connection in future work, as indicated in previous studies[1,2]. However, more in-depth mechanistic studies need to be conducted in this PCa phenotype, for which more model systems are required. Thus, these findings must be confirmed in *in vivo* studies, which is challenging due to the lack of a good CRPC-WNT xenograft model. Regardless, our data shows that it will be beneficial to assess SWI/SNF complex and MAPK-signaling interfering agents in a clinical setting to warrant their safety and efficacy for patients suffering from highly lethal variants of PCa.

Methods

Cell lines and compounds

PCa cell lines (LNCaP, 22Rv1, VCaP, PC3, DU145, NCI-H660, C4-2), other cell lines (HEK293T, DLD1) and benign prostate line (RWPE-1) were purchased from ATCC and maintained according to ATCC protocols. Patient-derived CRPC organoids (WCM and MSK) were established and maintained as organoids in Matrigel drops according to the previously described protocol[70]. LNCaP-AR cells were a kind gift from Dr. Sawyers and Dr. Mu (Memorial Sloan Kettering Cancer Center) and were cultured as previously described[5]. All used cell lines and their phenotype are listed in Supplementary Table 1. Cell cultures were regularly tested for *Mycoplasma* contamination and confirmed to be negative. Genentech Inc. synthesized A947, its epimer (A858), FHD-286 and AU-15330. Cobimetinib, Trametinib, VL285 and CHIR99021 were purchased from SelleckChem. BRM014 was purchased from MedChemExpress. All drugs used in this study are listed in Supplementary Table 2.

Western blot

Whole-cell lysates were prepared in 1x Cell lysis buffer (CST, 9803) supplemented with protease and phosphatase inhibitor cocktail (Thermo Fisher, 78440), and total protein was measured by Pierce BCA Protein Assay Kit (ThermoFisher Scientific, 23225). An equal amount of protein was loaded in SureBlot 10% or 4 to 15%, Bis-Tris Protein Gel (GenScript), and blotted. Subsequently, the nitrocellulose membrane was incubated with primary antibodies overnight in a cold room, shaking. Following incubation with HRP-conjugated secondary antibodies, membranes were imaged on a Vilber Fusion FX imager. Antibodies are listed in Supplementary Table 3.

Co-immunoprecipitation (Co-IP)

Co-IPs were performed using the Active Motif Co-IP Kit (Cat. No. 54002). Briefly, 200µg nuclear lysate was used per IP with Rabbit IgG isotype control (CST, 2729) or β-Catenin antibody (CST, 8480) at the concentration indicated by the supplier. After overnight rotation in a cold room, IPed lysate was incubated

for 2h with magnetic protein G beads. Beads were washed 3 times, and then IPed proteins were loaded on SDS-PAGE for detection using a native anti-rabbit HRP antibody (CST, 5127S). Antibodies are listed in Supplementary Table 3.

Proximity ligation assay (PLA)

Cells were cultured in 2D on 8-well chamber slides (polymer surface) at a density of 6.0×10^3 cells per well. After overnight attachment, cells were treated for 24h with 1µM of A858 or A947. PLA was carried out using the Duolink Proximity Ligation Assay Kit (DUO92101, Sigma) with beta-Catenin (NBP1-54467SS, Novus Biologicals) and TCF7L2 (MA5-32240, Thermo Fisher) or p-c-Jun antibody (9164, Cell Signalling) at a dilution of 1:200 overnight at 4 °C. Fluorescence signal was detected using the Leica DMI4000 microscope. Antibodies are listed in Supplementary Table 3.

Immunohistochemistry

Matrigel-extracted organoids were air-dried and subsequently baked at 62 °C for 25min. Immunohistochemistry (IHC) was performed on sections of formalin-fixed paraffin-embedded organoids (FFPE) using a Bond automated immunostainer and the Bond Polymer Refine detection system (Leica Microsystems, IL, USA) by the Translational Research Unit (TRU) platform, Bern. The TCF7L2 antibody (Cell Signaling Technologies, cat# 2569, Lot#5) was used for staining. The intensity of nuclear immunostaining was evaluated on whole slide sections by a pathologist (S.d.B.) blinded to additional pathological and clinical data.

Cell viability assay

Cells and organoids were plated in 2D onto coated 96-well plates in their respective culture medium and incubated at 37 °C in an atmosphere of 5% CO2. After overnight incubation, a serial dilution of compounds was prepared and added to the plate. The cells were further incubated for 7 days, and the CellTiter-Glo assay (Promega) was then performed according to the manufacturer's instructions to

determine cell proliferation. The luminescence signal from each well was acquired using the Varioskan LUX Plate Reader (Thermo Fisher), and the data were analyzed using GraphPad Prism software (GraphPad Software).

Classification of CRPC subtypes from publicly available tumor data

Table1. Publicly available datasets were analyzed in this study.

Dataset ID	Number of samples	Sample type	Sequencing platform and chemistry	Reference (DOI)
GSE137829	6	CRPC	10x Genomics 3' v2	10.1038/s42003-020-01476-1[46]
GSE143791	9	CRPC	10x Genomics 3' v2	10.1016/j.ccell.2021.09.005[47]
GSE157703	2	Primary tumor	10x Genomics 3' v3	10.1186/s12943-020-01264-9[50]
GSE181294	35	Primary tumor and normal adjacent tissue	10x Genomics 3' v2	10.1038/s41467-023-36325-2[49]
GSE193337	8	Primary tumor and normal adjacent tissue	10x Genomics 3' v3	10.1186/s12943-022-01597-7[48]
GSE210358	14	CRPC	10x Genomics 3' v3	10.1126/science.abn0478[2]

Raw data in FASTQ format were obtained from the respective sources (Table 1.) and aligned against the latest human (GRCh38) genome assembly release. Per-sample alignment and generation of feature-barcode matrices were carried out using the STAR-solo algorithm (STAR version 2.7.10b), tailored to the specific sequencing chemistry and the length of cell[71] barcodes and unique molecular identifiers (UMIs) on a case-by-case basis. We then imported the output feature-barcode matrices in an R environment (R version 4.0.2) and created individual Seurat objects for each sample (Seurat package version 4.0.3)[72-74]. A first round of quality filtering was performed through scuttle package (version 1.8.1)[75] by discarding outlier and low-quality cells after inspection of commonly used cell-level metrics (i.e., library size, UMI counts per cell, features detected per cell, mitochondrial and ribosomal counts ratio). Further doublet estimation and removal through the DoubletFinder prediction tool (version 2.0.3)[76] allowed us to drop unnecessary confounding technical artifacts. Thus, we merged our polished samples into a unique Seurat

object. Seurat global-scaling normalization and log-transformation method were applied to the complete expression matrix, followed by the selection of highly variable features and linear transformation to prepare the data for dimensional reduction. The latter scaling step also allowed us to regress out unwanted sources of heterogeneity, such as mitochondrial contamination and uneven library sizes. Thus, we determined the optimal number of principal components (PCs) as the lower dimension exhibiting a cumulative percentage of variation greater than 90% to be 82. Uniform manifold approximation and projection (UMAP) based on the previously selected PCs was used to reduce dimensionality and visualize the organization and clustering of cells. Specifically, we applied a graph-based unsupervised approach coupled with the Louvain clustering algorithm implemented in Seurat to generate cell clusters. We evaluated several levels of granularity through clustree (package version 0.5.0)[77] resolution stability analysis to accurately depict the intrinsic cellular heterogeneity. A clustering resolution of 1 was chosen, and markers identification was conducted by taking advantage of a hurdle model designed explicitly for scRNA-seq data and implemented in the MAST statistical framework[78], followed by a Bonferroni p-value adjustment to correct for multiple testing. Only genes expressed by at least 70% of cells in the cluster, displaying a significant adjusted p-value (pval_adj < 0.05) and a solid logarithmic fold change (log2FC > 1) were deemed as appropriate markers. After marker-based annotation of major cellular populations, we separated our collection, keeping only epithelial and malignant clusters, encompassing healthy/normal specimens of primary and castration-resistant tumors. The subsetted cells were again subjected to normalization and rescaling, and the relative UMAP was generated using 82 PCs, as before. Graph-based clustering was performed, and a granularity resolution of 0.3 was chosen, resulting in 34 clusters. In-depth annotation was assigned through marker identification. Therefore, we focused on determining which clusters could be associated with the activation of specific biological pathways by assessing the enrichment score (through *AddModuleScore* function) of some recently identified signatures[35] in the CRPC setting, such as AR, neuroendocrine (NE), stem-cell-like (SCL) and WNT-signaling. The Seurat object was then converted into an *anndata* object, and the Scanpy (version 1.9.5)[79] toolkit was used for visualization.

Transfection and siRNA-mediated Knockdown

ON-TARGET plus siRNA SMARTpool siRNAs against *SMARCA4 (L-010431-00-0005), SMARCA2 (L-017253-00-0005), CTNNB1 (L-003482-00-0005), TCF7L2 (L-003816-00-0005), CUL2 (L-007277-00-005) and control (D-001810-10-05)* were purchased from Dharmacon. siRNA pool against JUN and control were purchased from siTools. Reverse Transfection was performed in 6-well plates using the Lipofectamine 3000 reagent (Thermo Fisher Scientific) to the proportions of 2 µL of 20 µM siRNA per well. After overnight incubation, 5,000 cells were seeded triplicates in a clear 96-well plate, and confluence was monitored using IncuCyte S3 for up to 7 days. The remaining cells were harvested for protein extraction 96 h after Transfection.

siRNA rescue experiment

Rescue sequences (Supplementary Table 4) for the siTools against TCF7L2 (pool of 30 siRNAs) were designed and purchased from siTools Biotech. The rescue plasmid for TCF7L2 was synthesized and purchased from Atum Bio. Reverse Transfection of rescue plasmid was performed in 6-well plates using the Lipofectamine 3000 reagent (Thermo Fisher Scientific) to the proportions of 5 µL of 2 µg plasmid per well. After overnight incubation, cells were transfected with siTools TCF7L2 siRNA pool using the Lipofectamine RNAiMAX reagent (Thermo Fisher Scientific) to the proportions of 2 µL of 20nM siRNA per well. After overnight incubation, 5,000 cells were seeded triplicates in a clear 96-well plate, and confluence was monitored using IncuCyte S3 for up to 7 days. The remaining cells were harvested for protein extraction 96 h after Transfection. Sequences of siRNA and rescue sequence are shown Supplementary Table 4.

Lentiviral transduction of sgRNA into organoids

Organoids were transduced with CRISPRmod CRISPRi All-in-one Lentiviral hEF1a sgRNA against SMARCA4 particles (sgRNA1: VSGH12442-253241676, sgRNA2: VSGH12442-253150712, sgRNA3:

VSGH12442-253336788) or control (VSGC12547). Briefly, 5µl of concentrated virus was added to 500000 cells in suspension with TransDux MAX Lentivirus Transduction Reagent (SBI, LV860A-1) and spinfected at 600 x g, 1h, 32°C. Subsequently, they were incubated 4h at 37°C before careful seeding into Matrigel drops (50000 cells per drop) and topped up with appropriate media. Two days after transduction, virus-integrated cells were selected with puromycin.

Incucyte growth assays

2D monolayer formation

A total of 5,000 cells per well were seeded in clear 96-well plates. After overnight incubation, compounds were added at indicated concentrations. Plates were read in an IncuCyte S3. Every 6h, phase object confluence (percentage area) for cell growth was measured. Growth curves were visualized using GraphPad.

3D organoid formation

Twenty thousand cells per well were seeded in Matrigel drops using a clear 48-well plate. After 48h incubation, compounds were added at indicated concentrations. Plates were read in an IncuCyte SX5. Every 6h, organoid object count (µm2/image) for organoid formation was measured. Growth curves were visualized using GraphPad.

TOPFlash reporter assay

10000 cells were seeded in triplicate per condition in RSPO-free media in a 96-well format. After 24h, cells were transfected with 240ng TCF/LEF response reporter or control (BPS Biosciences, 60500). After 24h, cells were treated with indicated reagents and grown for another 24h at 37°C. Cells were then lysed, and FIREFLY luciferase and Renilla luciferase signals were detected using the TWO-step Luciferase assay system (BPS Biosciences, 60683). Luciferase was detected using the Varioskan LUX Plate Reader (Thermo Fisher).

RT-PCR

Cells were first seeded in 6cm-Petri dish and grown until they reached a confluency of approx. 90%. The cells were then treated with drug for 24h. Cells were then harvested for RNA isolation using the RNeasy Mini Kit (Qiagen). Synthesis of complementary DNAs (cDNAs) using FIREScript RT cDNA Synthesis Kit (Solis BioDyne) and real-time reverse transcription PCR (RT-PCR) assays using HOT FIREPol EvaGreen qPCR Mix Plus (Solis BioDyne) were performed using and applying the manufacturer protocols. Relative mRNA levels of each gene shown were normalized to the expression of the average of housekeeping genes GAPDH and ACTB. The sequences of the primers for qRT-PCR assays can be found in Supplementary Table 5.

Single-cell RNA-sequencing by SORT-seq library generation and analysis

SORT-seq was performed using Single Cell Discoveries (SCD) service. Organoids were treated for 72h with a control epimer (A858) or active compound (A947) at 1 µM, and 1x10e6 cells were harvested in PBS. Harvested cells were stained with 100ng/ml DAPI to stain dead cells. Using a cell sorter (conducted by Flow Cytometry Core, DBMR, Bern) and the recommended settings (Single Cell Discoveries B.V.), DAPI-negative cells were sorted as single cells in 376 wells of four 384-well plates containing immersion oil per condition. Resulting in a theoretical cell number of 1504 cells per condition. All post-harvesting steps were performed at 4°C. Plates were snap-frozen on dry ice for 15 minutes and sent out for sequencing at Single Cell Discoveries B.V.

Data were analyzed using the Seurat package v.4.3.0[80]. Cell QC filtering was done using the following thresholds: nCount > 4000, nFeature > 1000, percent.mito < 25, log10GenesPerUMI > 0.85. Differential gene expression analysis between clusters was done with Seurat::FindAllMarkers. Module scores were generated with Seurat::AddModuleScore. Gene set enrichment analysis was done with the package fgsea v.1.24.0[81] and the human gene sets from the Molecular Signatures Database (https://www.gsea-

msigdb.org). Gene regulatory networks analysis was done with pySCENIC v.0.12.1[82]. Overall analysis was done in R v.4.2.2.

RNA-seq library generation and processing

For bulk RNA-seq, organoids were treated with A858 or A947 (1µM) for 24h and 48h (3 biological replicates per condition). RNA was extracted using the RNeasy Kit (Qiagen); library generation and subsequent sequencing was performed by the clinical genomics lab (CGL) at the University of Bern. Sequencing reads were aligned against the human genome hg38 with STAR v.2.7.3a[83]. Gene counts were generated with RSEM v.1.3.2[84], whose index was generated using the GENCODE v33 primary assembly annotation. Differential gene expression analysis was done with DESeq2 v.1.34.0[85]. Gene set enrichment analysis was done with the package fgsea v.1.20.0[81] and the human gene sets from the Molecular Signatures Database (https://www.gsea-msigdb.org). Analysis was done in R v.4.1.2.

TCF7L2 ChIP-seq library generation and processing

For the ChIP-Seq assay, chromatin was prepared from 2 biological replicates of WCM1078 treated with A858 or A947 (1µM) for 24h, and ChIP-Seq assays were then performed by Active Motif Inc. using an antibody against TCF7L2 (Santa Cruz, cat# sc-8631, Lot# D0914). ChIP-seq sequence data was processed using an ENCODE-DC/chip-seq-pipeline2 -based workflow (https://github.com/ENCODE-DCC/chip-seq-pipeline2). Briefly, fastq files were aligned on the hg38 human genome reference using Bowtie2 (v2.2.6) followed by alignment sorting (samtools v1.7) of resulting bam files with filtering out of unmapped reads and keeping reads with mapping quality higher than 30. Duplicates were removed with Picard's MarkDuplicates (v1.126) function, followed by indexation of resulting bam files with samtools. For each bam file, genome coverage was computed with bedtools (v2.26.0), followed by the generation of bigwig (wigToBigWig v377) files. Peaks were called with macs2 (v2.2.4) for each treatment sample using a pooled input alignment (.bam file) as control. Downstream analyses were performed with DiffBind

v3.11.1 with default parameters, except for summits=250 in dba.count(). dba.contrast() and dba.analyzed() were used to compute significant differential peaks with DESeq2.

ATAC-seq library generation and processing

ATAC-seq was performed from 50'000 cryo-preserved cells per condition (1µM A858 and 1µM A947, n = 4 biological replicates) treated for 24h and analyzed as described in previous study[86]. Briefly, 50,000 cryo-preserved cells per condition were lysed for 5 minutes on ice and tagmented for 30 minutes at 37°C, followed by DNA isolation. DNA was barcoded and amplified before sequencing.

PRO-cap library generation and processing

For PRO-cap, approximately 30 million cells were processed per sample as previously described[87,88]. Library preparations for two biological replicates were performed separately. Cells were permeabilized, and run-on reactions were performed. After RNA isolation, two adaptor ligations and reverse transcription were performed with custom adaptors. Between adaptor ligations, cap state selection reactions were carried out using a series of enzymatic steps. RNA washes, phenol:chloroform extractions and ethanol precipitations were conducted between reactions. All steps were performed under RNase-free conditions. Libraries were sequenced on Illumina's NovaSeq lane following PCR amplification and library clean-up. Raw sequencing data was processed as previously described[89]. Briefly, sequencing data was trimmed with fastp version 0.22.0 and then aligned to the human genome (hg38) concatenated with EBV and human rDNA sequences (GenBank U13369.1) using STAR V2.7.10b. Raw alignments were filtered with samtools version 1.18 and deduplicated using umi_tools version 1.1.2. Alignments were converted to bigwig files using bedtools version 2.30.0 and kentUtils bedGraphToBigWig V2.8. Peaks were called using PINTS version 1.1.6[58]. Divergent peaks not overlapping with TSS +/-500 bp (GENCODE V37) were regarded as candidate enhancer RNAs.

Peaks were annotated with HOMER v.4.11 (http://homer.ucsd.edu/). Distal peaks were defined as those peaks in known introns and intergenic regions, and over 2 kb upstream or downstream from known transcription start sites. GIGGLE scores were generated at http://dbtoolkit.cistrome.org. Analysis was done in R v.4.2.2. Heatmaps were generated with deepTools v.3.5.0[90].

Acknowledgments

We thank the Translational Research Unit (TRU) and the Clinical Genomics Lab (CGL) of the University of Bern for their services. Further, we thank Charles Sawyers (Memorial Sloan Kettering) for the LNCaP-AR cell line. We thank Joanna Cyrta (Institut Curie, Paris) for her commentary and suggestions. We are grateful for the project funding by the Bern Centre for Precision Medicine (BCPM) and the Peter and Traudl Engelhorn Foundation. Scientific computing was partly performed on sciCORE - Scientific Computing Center at the University of Basel. Further, we acknowledge Mariana Ricca for her help editing and preparing this manuscript. We thank Michael Berlin at Arvinas Inc. for assistance with chemical synthesis.

Author Contributions

P.T. and M.A.R. conceived the project and designed all studies in the project. P.T., with assistance of P.D.R., A.N., and L.M., performed most experiments. M.S. performed ATAC-seq. A.B., X.Y., and Ju.T. are professional bioinformaticians and conducted data acquisition, analysis, and interpretation of RNA-seq, scRNA-seq, ATAC-seq, ChIP-seq, and GRO/PRO-cap. S.R.S. performed GRO/PRO-cap library preparation. A.K.L assisted with GRO/PRO-cap bioinformatic analysis. S.d.B conducted histopathological evaluation. Jo.T. performed histopathological data analysis. G.C. and M.B. performed bioinformatic CRPC signature score evaluation in scRNA-seq data curated from commercially available data. H.B. and Y.C. provided PCa organoid models. S.P. and C.N. provided expert commentary and bioinformatic expertise. H.Y. provided expert commentary and supervision of GRO/PRO-Cap

experiment. R.L.Y. provided resources, relevant data, and expert commentary. P.T. and M.A.R. wrote the manuscript with the help of Jo.T.

Competing interests

R.L.Y., X.Y., M.S., and Ju.T. are active employees of Genentech Inc. H.B. has served as consultant/advisory board member for Janssen, Astellas, Merck, Pfizer, Roche, Harpoon, Amgen, Bayer, Daiichi-Sankyo, Astra Zeneca, Harpoon and has received research funding (to institution) from Bristol Myers Squibb, Circle Pharma, Daiichi-Sankyo, Novartis. S.R.S. is an equity holder and member of the scientific advisory board of NeuScience, Inc., and a consultant at Third Bridge Group Limited. M.A.R has received research funding from Novartis, Roche, Ventana, Janssen, Astellas, and Eli Lilly and currently has a research collaboration agreement with Genentech Inc. M.A.R. is on the Scientific Advisory Board of Neogenomics Lab, is a Scientific Advisor and stockholder of Owkin, and co-founder of Verintas. M.A.R. is a co-inventor on prostate cancer patents in the diagnostic and treatment fields, including SWI/ SNF (Bern/Cornell). All other authors declare no competing interests.

References

1. Bluemn, E.G. *et al.* Androgen Receptor Pathway-Independent Prostate Cancer Is Sustained through FGF Signaling. *Cancer Cell* **32**, 474-489 e6 (2017).
2. Chan, J.M. *et al.* Lineage plasticity in prostate cancer depends on JAK/STAT inflammatory signaling. *Science* **377**, 1180-1191 (2022).
3. Beltran, H. *et al.* Divergent clonal evolution of castration-resistant neuroendocrine prostate cancer. *Nat Med* **22**, 298-305 (2016).
4. Ku, S.Y. *et al. Rb1* and *Trp53* cooperate to suppress prostate cancer lineage plasticity, metastasis, and antiandrogen resistance. *Science* **355**, 78 (2017).
5. Mu, P. *et al.* SOX2 promotes lineage plasticity and antiandrogen resistance in TP53- and RB1-deficient prostate cancer. *Science* **355**, 84-88 (2017).
6. Dardenne, E. *et al.* N-Myc Induces an EZH2-Mediated Transcriptional Program Driving Neuroendocrine Prostate Cancer. *Cancer Cell* **30**, 563-577 (2016).
7. Cyrta, J. *et al.* Role of specialized composition of SWI/SNF complexes in prostate cancer lineage plasticity. *Nature Communications* **11**, 5549 (2020).
8. Ye, Y., Chen, X. & Zhang, W. Mammalian SWI/SNF Chromatin Remodeling Complexes in Embryonic Stem Cells: Regulating the Balance Between Pluripotency and Differentiation. *Front Cell Dev Biol* **8**, 626383 (2020).
9. Hodges, C., Kirkland, J.G. & Crabtree, G.R. The Many Roles of BAF (mSWI/SNF) and PBAF Complexes in Cancer. *Cold Spring Harb Perspect Med* **6**(2016).
10. Rubin, M.A., Bristow, R.G., Thienger, P.D., Dive, C. & Imielinski, M. Impact of Lineage Plasticity to and from a Neuroendocrine Phenotype on Progression and Response in Prostate and Lung Cancers. *Molecular Cell* **80**, 562-577 (2020).
11. Xue, Y. *et al.* SMARCA4 loss is synthetic lethal with CDK4/6 inhibition in non-small cell lung cancer. *Nat Commun* **10**, 557 (2019).

12. Cantley, J. *et al.* Selective PROTAC-mediated degradation of SMARCA2 is efficacious in SMARCA4 mutant cancers. *Nat Commun* **13**, 6814 (2022).

13. Hoffman, G.R. *et al.* Functional epigenetics approach identifies BRM/SMARCA2 as a critical synthetic lethal target in BRG1-deficient cancers. *Proc Natl Acad Sci U S A* **111**, 3128-33 (2014).

14. He, T. *et al.* Targeting the mSWI/SNF Complex in POU2F-POU2AF Transcription Factor-Driven Malignancies. *bioRxiv* (2024).

15. Duplaquet, L. *et al.* Mammalian SWI/SNF complex activity regulates POU2F3 and constitutes a targetable dependency in small cell lung cancer. *bioRxiv*, 2024.01.21.576304 (2024).

16. Centore, R.C. *et al.* Pharmacologic inhibition of BAF chromatin remodeling complexes as a therapeutic approach to transcription factor-dependent cancers. *bioRxiv*, 2023.09.11.557162 (2023).

17. Wang, X. *et al.* BRD9 defines a SWI/SNF sub-complex and constitutes a specific vulnerability in malignant rhabdoid tumors. *Nat Commun* **10**, 1881 (2019).

18. McBride, M.J. *et al.* The SS18-SSX Fusion Oncoprotein Hijacks BAF Complex Targeting and Function to Drive Synovial Sarcoma. *Cancer Cell* **33**, 1128-1141 e7 (2018).

19. Banito, A. *et al.* The SS18-SSX Oncoprotein Hijacks KDM2B-PRC1.1 to Drive Synovial Sarcoma. *Cancer Cell* **33**, 527-541 e8 (2018).

20. Xiao, L. *et al.* Targeting SWI/SNF ATPases in enhancer-addicted prostate cancer. *Nature* **601**, 434-439 (2022).

21. Zhang, J. *et al.* Structure-based identification of new orally bioavailable BRD9-PROTACs for treating acute myelocytic leukemia. *European Journal of Medicinal Chemistry* **262**, 115872 (2023).

22. Griffin, C.T., Curtis, C.D., Davis, R.B., Muthukumar, V. & Magnuson, T. The chromatin-remodeling enzyme BRG1 modulates vascular Wnt signaling at two levels. *Proc Natl Acad Sci U S A* **108**, 2282-7 (2011).

23. Park, J.I. *et al.* Telomerase modulates Wnt signalling by association with target gene chromatin. *Nature* **460**, 66-72 (2009).

24. Wang, Y. *et al.* The long noncoding RNA lncTCF7 promotes self-renewal of human liver cancer stem cells through activation of Wnt signaling. *Cell Stem Cell* **16**, 413-25 (2015).

25. Murillo-Garzon, V. & Kypta, R. WNT signalling in prostate cancer. *Nat Rev Urol* **14**, 683-696 (2017).

26. Miyamoto, D.T. *et al.* RNA-Seq of single prostate CTCs implicates noncanonical Wnt signaling in antiandrogen resistance. *Science* **349**, 1351-6 (2015).

27. Korinek, V. *et al.* Constitutive transcriptional activation by a beta-catenin-Tcf complex in APC-/- colon carcinoma. *Science* **275**, 1784-7 (1997).

28. Zhan, T., Rindtorff, N. & Boutros, M. Wnt signaling in cancer. *Oncogene* **36**, 1461-1473 (2017).

29. Su, L.K., Vogelstein, B. & Kinzler, K.W. Association of the APC tumor suppressor protein with catenins. *Science* **262**, 1734-7 (1993).

30. Rubinfeld, B. *et al.* Association of the APC gene product with beta-catenin. *Science* **262**, 1731-4 (1993).

31. Sandsmark, E. *et al.* A novel non-canonical Wnt signature for prostate cancer aggressiveness. *Oncotarget* **8**, 9572-9586 (2017).

32. Grasso, C.S. *et al.* The mutational landscape of lethal castration-resistant prostate cancer. *Nature* **487**, 239-43 (2012).

33. Zong, Y. *et al.* Stromal epigenetic dysregulation is sufficient to initiate mouse prostate cancer via paracrine Wnt signaling. *Proc Natl Acad Sci U S A* **109**, E3395-404 (2012).

34. Li, X. *et al.* Prostate tumor progression is mediated by a paracrine TGF-beta/Wnt3a signaling axis. *Oncogene* **27**, 7118-30 (2008).

35. Tang, F. *et al.* Chromatin profiles classify castration-resistant prostate cancers suggesting therapeutic targets. *Science* **376**, eabe1505 (2022).

36. Tierney, M.T. *et al.* Vitamin A resolves lineage plasticity to orchestrate stem cell lineage choices. *Science* **383**, eadi7342 (2024).

37. Ge, Y. *et al.* Stem Cell Lineage Infidelity Drives Wound Repair and Cancer. *Cell* **169**, 636-650 e14 (2017).

38. Adam, R.C. *et al.* Pioneer factors govern super-enhancer dynamics in stem cell plasticity and lineage choice. *Nature* **521**, 366-70 (2015).

39. Nateri, A.S., Spencer-Dene, B. & Behrens, A. Interaction of phosphorylated c-Jun with TCF4 regulates intestinal cancer development. *Nature* **437**, 281-5 (2005).

40. Toualbi, K. *et al.* Physical and functional cooperation between AP-1 and beta-catenin for the regulation of TCF-dependent genes. *Oncogene* **26**, 3492-502 (2007).

41. Mann, B. *et al.* Target genes of beta-catenin-T cell-factor/lymphoid-enhancer-factor signaling in human colorectal carcinomas. *Proc Natl Acad Sci U S A* **96**, 1603-8 (1999).

42. Hankey, W. *et al.* Chromatin-associated APC regulates gene expression in collaboration with canonical WNT signaling and AP-1. *Oncotarget* **9**, 31214-31230 (2018).

43. Ding, Y. *et al.* Chromatin remodeling ATPase BRG1 and PTEN are synthetic lethal in prostate cancer. *The Journal of Clinical Investigation* **129**, 759-773 (2019).

44. Zhang, L., Riley-Gillis, B., Vijay, P. & Shen, Y. Acquired Resistance to BET-PROTACs (Proteolysis-Targeting Chimeras) Caused by Genomic Alterations in Core Components of E3 Ligase Complexes. *Mol Cancer Ther* **18**, 1302-1311 (2019).

45. Ottis, P. *et al.* Cellular Resistance Mechanisms to Targeted Protein Degradation Converge Toward Impairment of the Engaged Ubiquitin Transfer Pathway. *ACS Chem Biol* **14**, 2215-2223 (2019).

46. Dong, B. *et al.* Single-cell analysis supports a luminal-neuroendocrine transdifferentiation in human prostate cancer. *Commun Biol* **3**, 778 (2020).

47. Kfoury, Y. *et al.* Human prostate cancer bone metastases have an actionable immunosuppressive microenvironment. *Cancer Cell* **39**, 1464-1478 e8 (2021).

48. Heidegger, I. *et al.* Comprehensive characterization of the prostate tumor microenvironment identifies CXCR4/CXCL12 crosstalk as a novel antiangiogenic therapeutic target in prostate cancer. *Mol Cancer* **21**, 132 (2022).

49. Hirz, T. *et al.* Dissecting the immune suppressive human prostate tumor microenvironment via integrated single-cell and spatial transcriptomic analyses. *Nat Commun* **14**, 663 (2023).

50. Ma, X. *et al.* Identification of a distinct luminal subgroup diagnosing and stratifying early stage prostate cancer by tissue-based single-cell RNA sequencing. *Mol Cancer* **19**, 147 (2020).

51. Muraro, M.J. *et al.* A Single-Cell Transcriptome Atlas of the Human Pancreas. *Cell Syst* **3**, 385-394 e3 (2016).

52. Aibar, S. *et al.* SCENIC: single-cell regulatory network inference and clustering. *Nat Methods* **14**, 1083-1086 (2017).

53. Gong, A. & Huang, S. FoxM1 and Wnt/beta-catenin signaling in glioma stem cells. *Cancer Res* **72**, 5658-62 (2012).

54. Zhang, N. *et al.* FoxM1 promotes beta-catenin nuclear localization and controls Wnt target-gene expression and glioma tumorigenesis. *Cancer Cell* **20**, 427-42 (2011).

55. Veeman, M.T., Slusarski, D.C., Kaykas, A., Louie, S.H. & Moon, R.T. Zebrafish prickle, a modulator of noncanonical Wnt/Fz signaling, regulates gastrulation movements. *Curr Biol* **13**, 680-5 (2003).

56. Schick, S. *et al.* Acute BAF perturbation causes immediate changes in chromatin accessibility. *Nat Genet* **53**, 269-278 (2021).

57. Iurlaro, M. *et al.* Mammalian SWI/SNF continuously restores local accessibility to chromatin. *Nat Genet* **53**, 279-287 (2021).

58. Yao, L. *et al.* A comparison of experimental assays and analytical methods for genome-wide identification of active enhancers. *Nat Biotechnol* **40**, 1056-1065 (2022).

59. Tippens, N.D. *et al.* Transcription imparts architecture, function and logic to enhancer units. *Nat Genet* **52**, 1067-1075 (2020).

60. Layer, R.M. *et al.* GIGGLE: a search engine for large-scale integrated genome analysis. *Nat Methods* **15**, 123-126 (2018).

61. Labbe, D.P. & Brown, M. Transcriptional Regulation in Prostate Cancer. *Cold Spring Harb Perspect Med* **8**(2018).

62. Yamada, Y. & Beltran, H. Clinical and Biological Features of Neuroendocrine Prostate Cancer. *Curr Oncol Rep* **23**, 15 (2021).

63. Neiheisel, A., Kaur, M., Ma, N., Havard, P. & Shenoy, A.K. Wnt pathway modulators in cancer therapeutics: An update on completed and ongoing clinical trials. *Int J Cancer* **150**, 727-740 (2022).

64. Luo, M. *et al.* Advances of targeting the YAP/TAZ-TEAD complex in the hippo pathway for the treatment of cancers. *Eur J Med Chem* **244**, 114847 (2022).

65. Haffner, M.C. *et al.* Genomic and phenotypic heterogeneity in prostate cancer. *Nat Rev Urol* **18**, 79-92 (2021).

66. Comandante-Lou, N., Baumann, D.G. & Fallahi-Sichani, M. AP-1 transcription factor network explains diverse patterns of cellular plasticity in melanoma cells. *Cell Rep* **40**, 111147 (2022).

67. Shaulian, E. & Karin, M. AP-1 in cell proliferation and survival. *Oncogene* **20**, 2390-400 (2001).

68. Nickols, N.G. *et al.* MEK-ERK signaling is a therapeutic target in metastatic castration resistant prostate cancer. *Prostate Cancer Prostatic Dis* **22**, 531-538 (2019).

69. Kirk, J.S. *et al.* Integrated single-cell analysis defines the epigenetic basis of castration-resistant prostate luminal cells. *bioRxiv*, 2023.03.03.530998 (2023).

70. Gao, D. *et al.* Organoid cultures derived from patients with advanced prostate cancer. *Cell* **159**, 176-187 (2014).

71. Kaminow, B., Yunusov, D. & Dobin, A. STARsolo: accurate, fast and versatile mapping/quantification of single-cell and single-nucleus RNA-seq data. *bioRxiv*, 2021.05.05.442755 (2021).

72. Stuart, T. *et al.* Comprehensive Integration of Single-Cell Data. *Cell* **177**, 1888-1902 e21 (2019).

73. Butler, A., Hoffman, P., Smibert, P., Papalexi, E. & Satija, R. Integrating single-cell transcriptomic data across different conditions, technologies, and species. *Nat Biotechnol* **36**, 411-420 (2018).

74. Satija, R., Farrell, J.A., Gennert, D., Schier, A.F. & Regev, A. Spatial reconstruction of single-cell gene expression data. *Nat Biotechnol* **33**, 495-502 (2015).

75. McCarthy, D.J., Campbell, K.R., Lun, A.T. & Wills, Q.F. Scater: pre-processing, quality control, normalization and visualization of single-cell RNA-seq data in R. *Bioinformatics* **33**, 1179-1186 (2017).

76. McGinnis, C.S., Murrow, L.M. & Gartner, Z.J. DoubletFinder: Doublet Detection in Single-Cell RNA Sequencing Data Using Artificial Nearest Neighbors. *Cell Syst* **8**, 329-337 e4 (2019).

77. Zappia, L. & Oshlack, A. Clustering trees: a visualization for evaluating clusterings at multiple resolutions. *Gigascience* **7**(2018).

78. Finak, G. *et al.* MAST: a flexible statistical framework for assessing transcriptional changes and characterizing heterogeneity in single-cell RNA sequencing data. *Genome Biol* **16**, 278 (2015).

79. Wolf, F.A., Angerer, P. & Theis, F.J. SCANPY: large-scale single-cell gene expression data analysis. *Genome Biol* **19**, 15 (2018).

80. Hao, Y. *et al.* Integrated analysis of multimodal single-cell data. *Cell* **184**, 3573-3587 e29 (2021).

81. Korotkevich, G. *et al.* Fast gene set enrichment analysis. *bioRxiv*, 060012 (2021).

82. Van de Sande, B. *et al.* A scalable SCENIC workflow for single-cell gene regulatory network analysis. *Nat Protoc* **15**, 2247-2276 (2020).

83. Dobin, A. *et al.* STAR: ultrafast universal RNA-seq aligner. *Bioinformatics* **29**, 15-21 (2012).

84. Li, B. & Dewey, C.N. RSEM: accurate transcript quantification from RNA-Seq data with or without a reference genome. *BMC Bioinformatics* **12**, 323 (2011).

85. Love, M.I., Huber, W. & Anders, S. Moderated estimation of fold change and dispersion for RNA-seq data with DESeq2. *Genome Biol* **15**, 550 (2014).

86. Hagenbeek, T.J. *et al.* An allosteric pan-TEAD inhibitor blocks oncogenic YAP/TAZ signaling and overcomes KRAS G12C inhibitor resistance. *Nat Cancer* **4**, 812-828 (2023).

87. Kwak, H., Fuda, N.J., Core, L.J. & Lis, J.T. Precise maps of RNA polymerase reveal how promoters direct initiation and pausing. *Science* **339**, 950-3 (2013).

88. Mahat, D.B. *et al.* Base-pair-resolution genome-wide mapping of active RNA polymerases using precision nuclear run-on (PRO-seq). *Nature Protocols* **11**, 1455-1476 (2016).

89. Cotter, K.A. *et al.* Capped nascent RNA sequencing reveals novel therapy-responsive enhancers in prostate cancer. *bioRxiv*, 2022.04.08.487666 (2022).

90. Ramirez, F. *et al.* deepTools2: a next generation web server for deep-sequencing data analysis. *Nucleic Acids Res* **44**, W160-5 (2016).

Figure 1

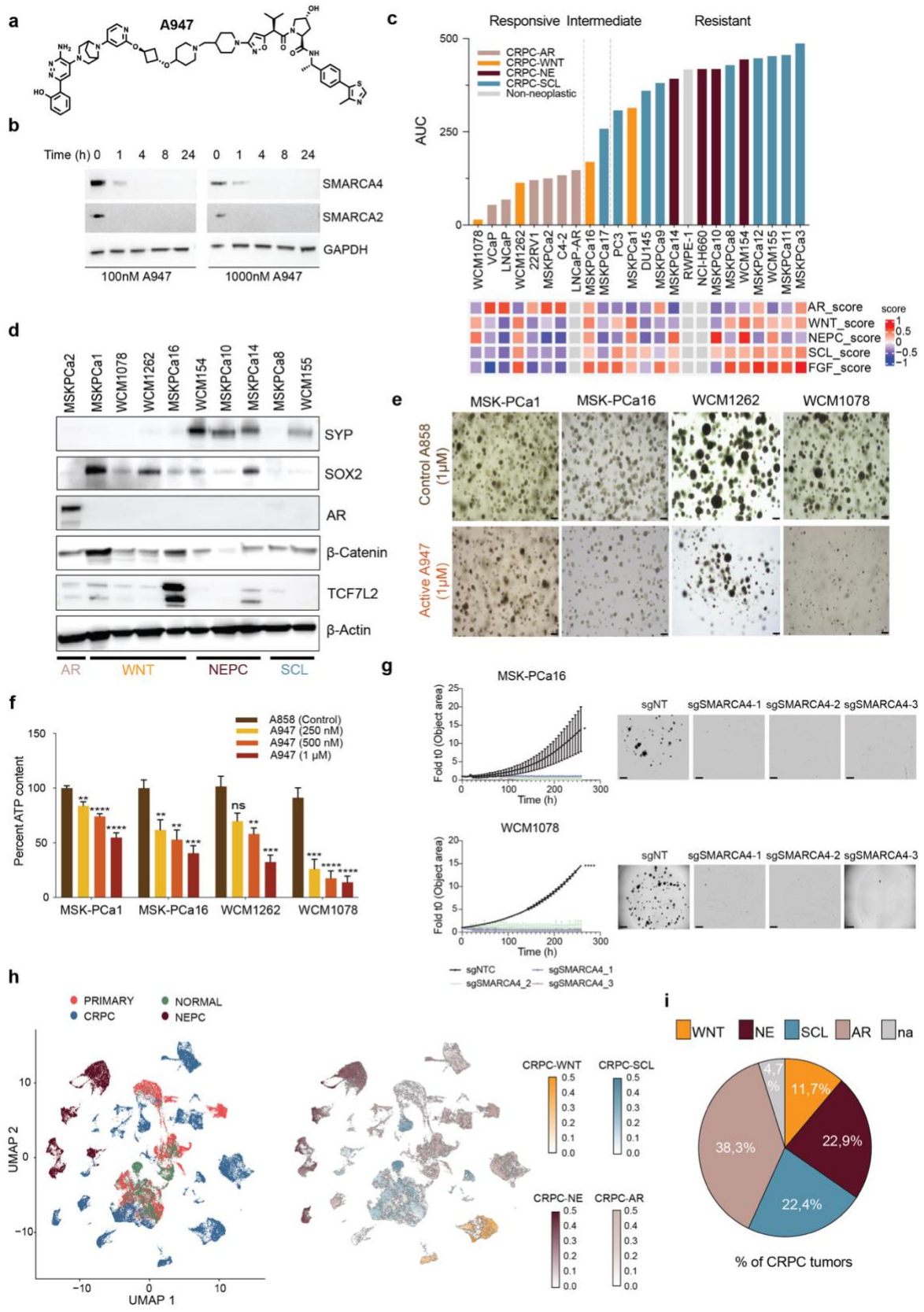
a
A947
b
Time (h) 0 1 4 8 24 0 1 4 8 24
SMARCA4
SMARCA2
GAPDH
100nM A947
1000nM A947
c
Responsive Intermediate Resistant
CRPC-AR
CRPC-WNT
CRPC-NE
CRPC-SCL
Non-neoplastic
AUC
WCM1078 VCaP LNCaP WCM1262 22RV1 MSKPCa2 C4-2 LNCaP-AR MSKPCa16 MSKPCa17 PC3 MSKPCa1 DU145 MSKPCa9 MSKPCa14 RWPE-1 NCI-H660 MSKPCa10 MSKPCa8 WCM154 MSKPCa12 WCM155 MSKPCa11 MSKPCa3
AR_score
WNT_score
NEPC_score
SCL_score
FGF_score
score
d
MSKPCa2 MSKPCa1 WCM1078 WCM1262 MSKPCa16 WCM154 MSKPCa10 MSKPCa14 MSKPCa8 WCM155
SYP
SOX2
AR
β-Catenin
TCF7L2
β-Actin
AR WNT NEPC SCL
e
MSK-PCa1 MSK-PCa16 WCM1262 WCM1078
Control A858 (1μM)
Active A947 (1μM)
f
A858 (Control)
A947 (250 nM)
A947 (500 nM)
A947 (1 μM)
Percent ATP content
MSK-PCa1 MSK-PCa16 WCM1262 WCM1078
g
MSK-PCa16
WCM1078
Fold t0 (Object area)
Time (h)
sgNT sgSMARCA4-1 sgSMARCA4-2 sgSMARCA4-3
sgNTC
sgSMARCA4_1
sgSMARCA4_2
sgSMARCA4_3
h
PRIMARY
CRPC
NORMAL
NEPC
UMAP 1
UMAP 2
CRPC-WNT
CRPC-SCL
CRPC-NE
CRPC-AR
i
WNT NE SCL AR na
11,7%
22,9%
22,4%
38,3%
4,7 %
% of CRPC tumors

Fig.1 Drug screen identifies SMARCA2/4 as a vulnerability in DNPC cell models

a, Structure of A947 SMARCA2/4 PROTAC degrader.

b, Immunoblot of indicated proteins in HEK293 cells treated with A947 (0.1µM or 1µM) or DMSO over indicated time course. GAPDH represents loading control and is probed in a representative immunoblot.

c, Area under the curve (AUC) of A947 in a panel of human-derived prostate cancer or normal cell lines after 7 days of treatment. Heatmap indicates gene-set scores per cell model using Tang et al.[35] scores.

d, Immunoblot of indicated proteins in a panel of PCa organoids representing different phenotypes. β-Actin serves as a loading control and is probed in a representative immunoblot.

e, Brightfield microscopy of indicated PCa organoids after 10 days of treatment with A947 (1µM) or epimer control A858 (1µM). Scale bars: 20 µm.

f, Proliferation of indicated PCa organoids after 10 days of treatment with A947 (at 0.25µM, 0.5µM, 1µM) or epimer control A858 (1µM) measured by Celltiter Glo 3D ($n = 3$ independent biological experiments). Data are presented as mean values +/− SEM and analyzed using two-way ANOVA (*$p < 0.05$, **$p < 0.01$, ***$p < 0.001$, ****$p < 0.0001$).

g, Spheroid formation of indicated PCa organoids transduced with CRISPRi-Cas9 guide RNA (sgRNA) against SMARCA4 measured by live imaging using Incucyte SX5. $N = 3$ independent experiments. Brightfield microscopy of indicated PCa organoids at Incucyte assay endpoint, Scale bars: 800 µm. Data are presented as mean values +/− SEM and analyzed using two-way ANOVA (*$p < 0.05$, **$p < 0.01$, ***$p < 0.001$, ****$p < 0.0001$).

h, UMAP plot showing disease classification (left) and relative expression of indicated signature gene scores (right) in 74 samples from six distinct PCa scRNAseq studies[2,46-50]. Side annotations indicate the AR score, NE score, stem cell-like (SCL) score, and WNT score, as determined by Tang et al.[35], compared with pathology classification and molecular subtypes of each sample. False discovery rate (FDR) <0.05.

i, Percentage of indicated signatures found among all CRPC classified samples displayed as a pie chart. Not announced (na).

Figure 2

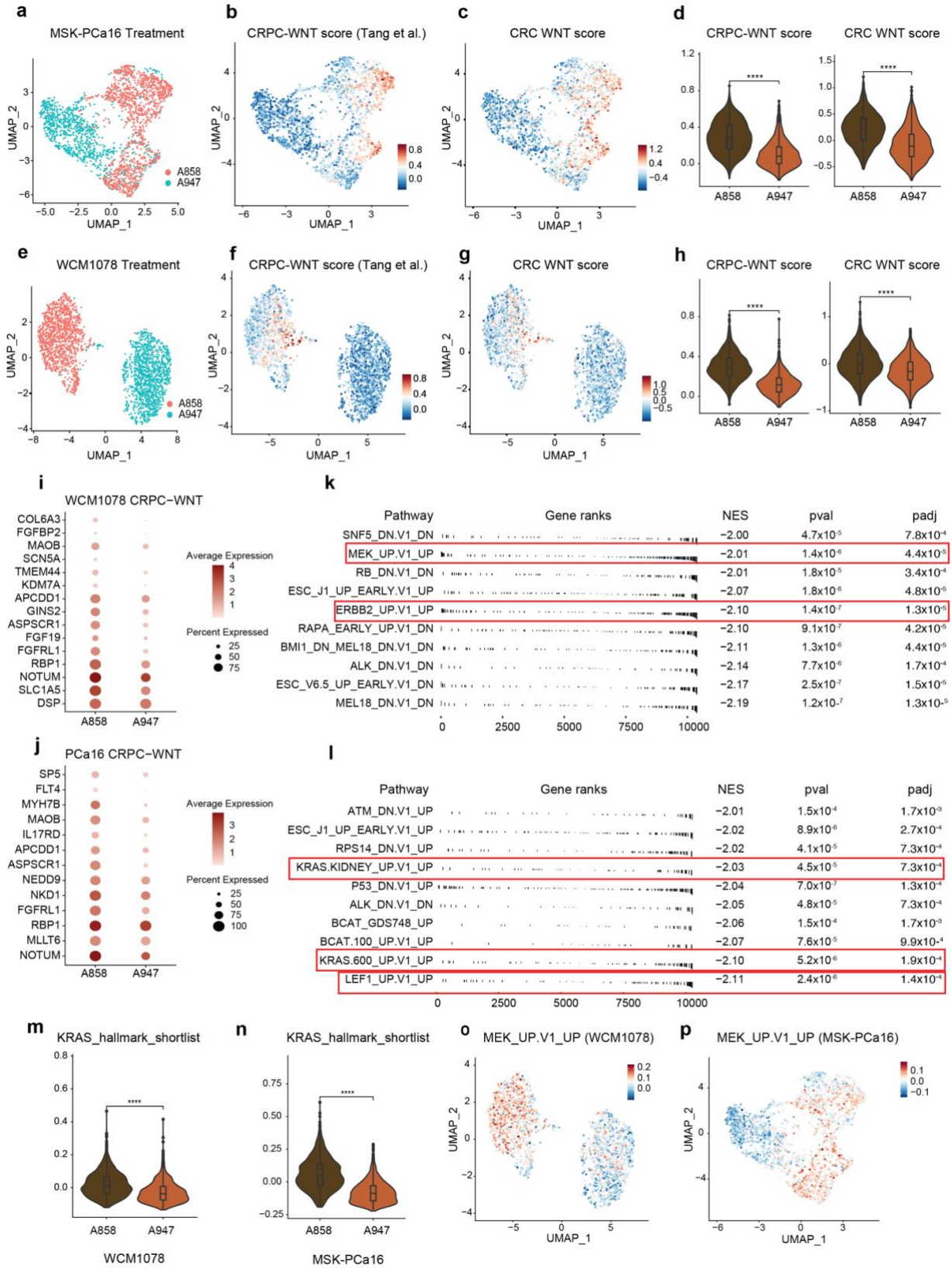
a
MSK-PCa16 Treatment
A858
A947
UMAP_1
UMAP_2
b
CRPC-WNT score (Tang et al.)
c
CRC WNT score
d
CRPC-WNT score
CRC WNT score
A858
A947
e
WCM1078 Treatment
f
CRPC-WNT score (Tang et al.)
g
CRC WNT score
h
CRPC-WNT score
CRC WNT score
i
WCM1078 CRPC−WNT
COL6A3
FGFBP2
MAOB
SCN5A
TMEM44
KDM7A
APCDD1
GINS2
ASPSCR1
FGF19
FGFRL1
RBP1
NOTUM
SLC1A5
DSP
Average Expression
Percent Expressed
A858
A947
j
PCa16 CRPC−WNT
SP5
FLT4
MYH7B
MAOB
IL17RD
APCDD1
ASPSCR1
NEDD9
NKD1
FGFRL1
RBP1
MLLT6
NOTUM
Average Expression
Percent Expressed
A858
A947
k
Pathway
Gene ranks
NES
pval
padj
SNF5_DN.V1_DN −2.00 4.7x10-5 7.8x10-4
MEK_UP.V1_UP −2.01 1.4x10-6 4.4x10-5
RB_DN.V1_DN −2.01 1.8x10-5 3.4x10-4
ESC_J1_UP_EARLY.V1_UP −2.07 1.8x10-6 4.8x10-5
ERBB2_UP.V1_UP −2.10 1.4x10-7 1.3x10-5
RAPA_EARLY_UP.V1_DN −2.10 9.1x10-7 4.2x10-5
BMI1_DN_MEL18_DN.V1_DN −2.11 1.3x10-6 4.4x10-5
ALK_DN.V1_DN −2.14 7.7x10-6 1.7x10-4
ESC_V6.5_UP_EARLY.V1_DN −2.17 2.5x10-7 1.5x10-5
MEL18_DN.V1_DN −2.19 1.2x10-7 1.3x10-5
0
2500
5000
7500
10000
l
Pathway
Gene ranks
NES
pval
padj
ATM_DN.V1_UP −2.01 1.5x10-4 1.7x10-3
ESC_J1_UP_EARLY.V1_UP −2.02 8.9x10-6 2.7x10-4
RPS14_DN.V1_UP −2.02 4.1x10-5 7.3x10-4
KRAS.KIDNEY_UP.V1_UP −2.03 4.5x10-5 7.3x10-4
P53_DN.V1_UP −2.04 7.0x10-7 1.3x10-4
ALK_DN.V1_DN −2.05 4.8x10-5 7.3x10-4
BCAT_GDS748_UP −2.06 1.5x10-4 1.7x10-3
BCAT.100_UP.V1_UP −2.07 7.6x10-5 9.9x10-4
KRAS.600_UP.V1_UP −2.10 5.2x10-6 1.9x10-4
LEF1_UP.V1_UP −2.11 2.4x10-6 1.4x10-4
0
2500
5000
7500
10000
m
KRAS_hallmark_shortlist
A858
A947
WCM1078
n
KRAS_hallmark_shortlist
A858
A947
MSK-PCa16
o
MEK_UP.V1_UP (WCM1078)
UMAP_1
UMAP_2
p
MEK_UP.V1_UP (MSK-PCa16)
UMAP_1
UMAP_2

Fig. 2 SMARCA2/4 degradation leads to strong downregulation of lineage-characterizing CRPC-WNT signature

a, UMAP plot of MSK-PCa16 organoids treated with either 1µM A858 (red) or 1µM A947 (teal) after 72h.

b, UMAP plot of MSK-PCa16 organoids treated with either 1µM A858 or 1µM A947 after 72h displaying CRPC-WNT signature score[35].

c, UMAP plot of MSK-PCa16 organoids treated with either 1µM A858 or 1µM A947 after 72h displaying CRC WNT signature score.

d, Violin plot of MSK-PCa16 organoids treated with either 1µM A858 or 1µM A947 after 72h displaying CRPC-WNT signature[35] and CRC WNT signature score. Analyzed using the Wilcoxon test (****$p < 0.0001$).

e, UMAP plot of WCM1078 organoids treated with either 1µM A858 (red) or 1µM A947 (teal) after 72h.

f, UMAP plot of WCM1078 organoids treated with either 1µM A858 or 1µM A947 after 72h displaying CRPC-WNT signature score[35].

g, UMAP plot of WCM1078 organoids treated with either 1µM A858 or 1µM A947 after 72h displaying CRC WNT signature score.

h, Violin plot of MSK-PCa16 organoids treated with either 1µM A858 or 1µM A947 after 72h displaying CRPC-WNT signature[35] and CRC WNT signature score. Analyzed using the Wilcoxon test (****$p < 0.0001$).

i, Bubble plot of top 10 deregulated CRPC-WNT signature genes[35] in WCM1078 organoids treated with either 1µM A858 or 1µM A947 after 72h.

j, Bubble plot of top 10 deregulated CRPC-WNT signature genes[35] in MSK-PCa16 organoids treated with either 1µM A858 or 1µM A947 after 72h.

k, GSEA of C6 oncogenic gene sets in WCM1078 organoids treated with either 1µM A858 or 1µM A947 after 72h.

l, GSEA of C6 oncogenic gene sets in MSK-PCa16 organoids treated with either 1µM A858 or 1µM A947 after 72h.

m, Violin plot of hallmark KRAS signature in WCM1078 organoids treated with either 1µM A858 or 1µM A947 after 72h. Analyzed using the Wilcoxon test (****$p < 0.0001$).

n, Violin plot of hallmark KRAS signature in MSK-PCa16 organoids treated with either 1µM A858 or 1µM A947 after 72h. Analyzed using the Wilcoxon test (****$p < 0.0001$).

o, UMAP plot of WCM1078 organoids treated with either 1µM A858 or 1µM A947 after 72h displaying C6.oncogenic signature MEK_UP.V1_UP.

p, UMAP plot of MSK-PCa16 organoids treated with either 1µM A858 or 1µM A947 after 72h displaying C6.oncogenic signature MEK_UP.V1_UP.

Figure 3

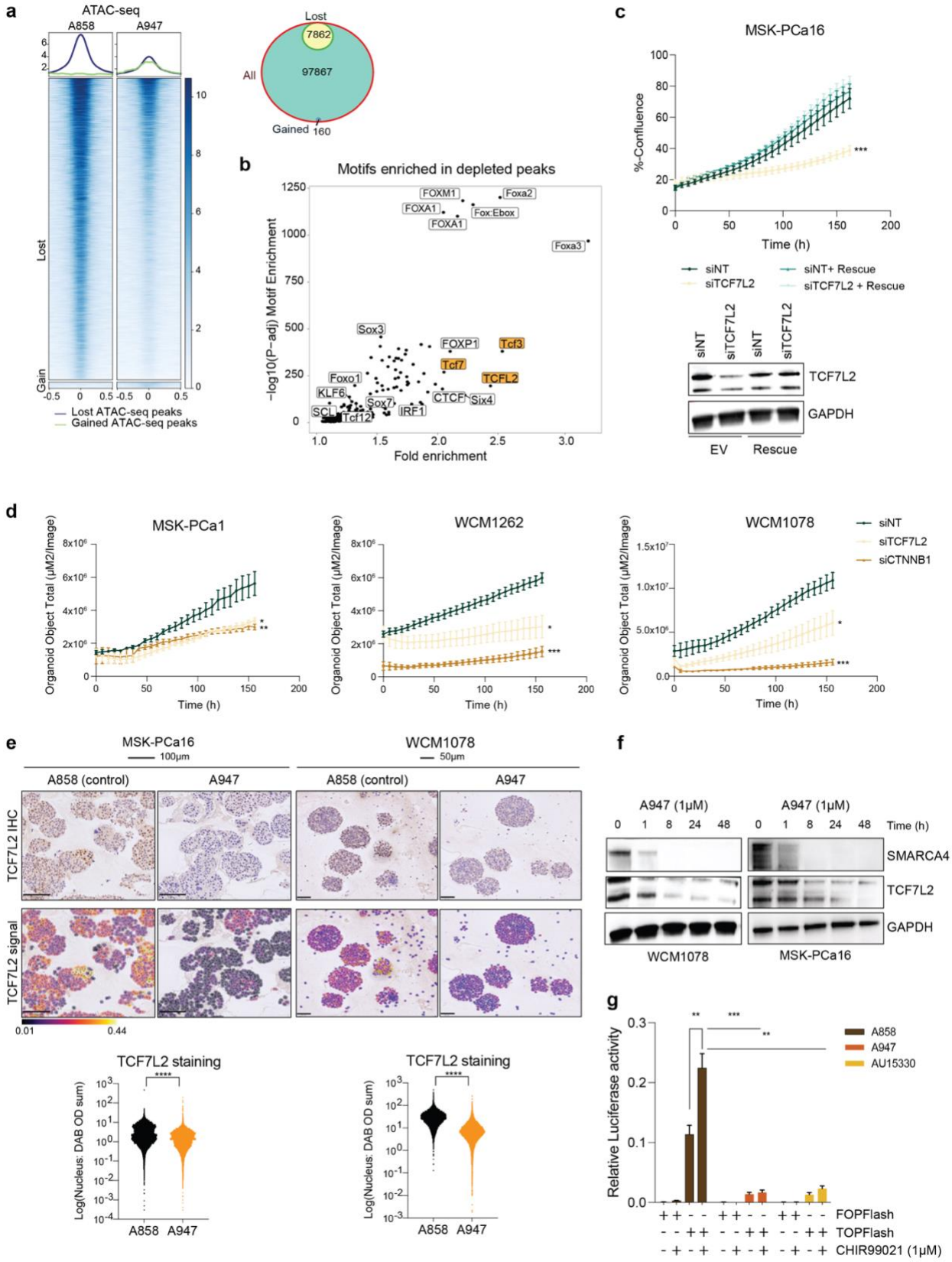
a
ATAC-seq
A858
A947
Lost
Gain
Lost ATAC-seq peaks
Gained ATAC-seq peaks
Lost
7862
All
97867
Gained
160
b
Motifs enriched in depleted peaks
−log10(P−adj) Motif Enrichment
Fold enrichment
FOXM1
Foxa2
FOXA1
Fox:Ebox
FOXA1
Foxa3
Sox3
FOXP1
Tcf3
Tcf7
Foxo1
TCFL2
KLF6
CTCF
Six4
Sox7
SCL
Tcf12
IRF1
c
MSK-PCa16
%-Confluence
Time (h)
siNT
siTCF7L2
siNT+ Rescue
siTCF7L2 + Rescue
siNT
siTCF7L2
siNT
siTCF7L2
TCF7L2
GAPDH
EV
Rescue
d
MSK-PCa1
WCM1262
WCM1078
Organoid Object Total (µM2/Image)
Time (h)
siNT
siTCF7L2
siCTNNB1
e
MSK-PCa16
100µm
WCM1078
50µm
A858 (control)
A947
A858 (control)
A947
TCF7L2 IHC
TCF7L2 signal
0.01
0.44
TCF7L2 staining
Log(Nucleus: DAB OD sum)
A858
A947
TCF7L2 staining
Log(Nucleus: DAB OD sum)
A858
A947
f
A947 (1µM)
A947 (1µM)
0
1
8
24
48
0
1
8
24
48
Time (h)
SMARCA4
TCF7L2
GAPDH
WCM1078
MSK-PCa16
g
Relative Luciferase activity
A858
A947
AU15330
FOPFlash
TOPFlash
CHIR99021 (1µM)

Fig.3 PROTAC-mediated degradation of SMARCA2/4 closes TCF chromatin binding site and restricts TCF7L2 abundance

a, ATAC-seq read-density tornado plots from WCM1078 organoids treated with 1μM A858 or 1μM A947 for 24h (n = 4 biological replicates). Venn diagram indicating lost and gained regions.

b, Motifs enriched in depleted peaks from WCM1078 treated for 24h with 1μM A947 identified using HOMER on ATAC-seq.

c, Growth data measured by live-cell imaging (Incucyte S3) upon transfection of indicated siRNA or plasmid (EV or rescue). Immunoblot of indicated proteins at 72h after transfection. GAPDH serves as loading control. Data are presented as mean values +/− SEM and analyzed using two-way ANOVA (*$p < 0.05$, **$p < 0.01$, ***$p < 0.001$). EV: empty vector.

d, Spheroid formation measured by live-cell imaging (Incucyte SX5) upon transfection of indicated siRNA. Data are presented as mean values +/− SEM and analyzed using two-way Anova (*$p < 0.05$, **$p < 0.01$, ***$p < 0.001$).

e, Immunohistochemistry (IHC) and staining intensity of TCF7L2 on indicated organoids upon treatment with 1μM A858 or 1μM A947 for 24h. Violin plot from TCF7L2 staining intensity analyzed using two-way ANOVA (*$p < 0.05$, **$p < 0.01$, ***$p < 0.001$, ****$p < 0.0001$). Scale: 100μm (MSK-PCa16), 50μm (WCM1078).

f, Immunoblot of indicated proteins at indicated time upon treatment with 1μM A947. GAPDH serves as loading control.

g, TOPFlash TCF/LEF reporter assay measured after 48h upon transfection and 24h upon treatment with indicated drugs in MSK-PCa16. FOPFlash serves as a negative control. Data are presented as mean values +/− SEM and analyzed using Students t-test (ns= not significant, *$p < 0.05$, **$p < 0.01$, ***$p < 0.001$).

Figure 4

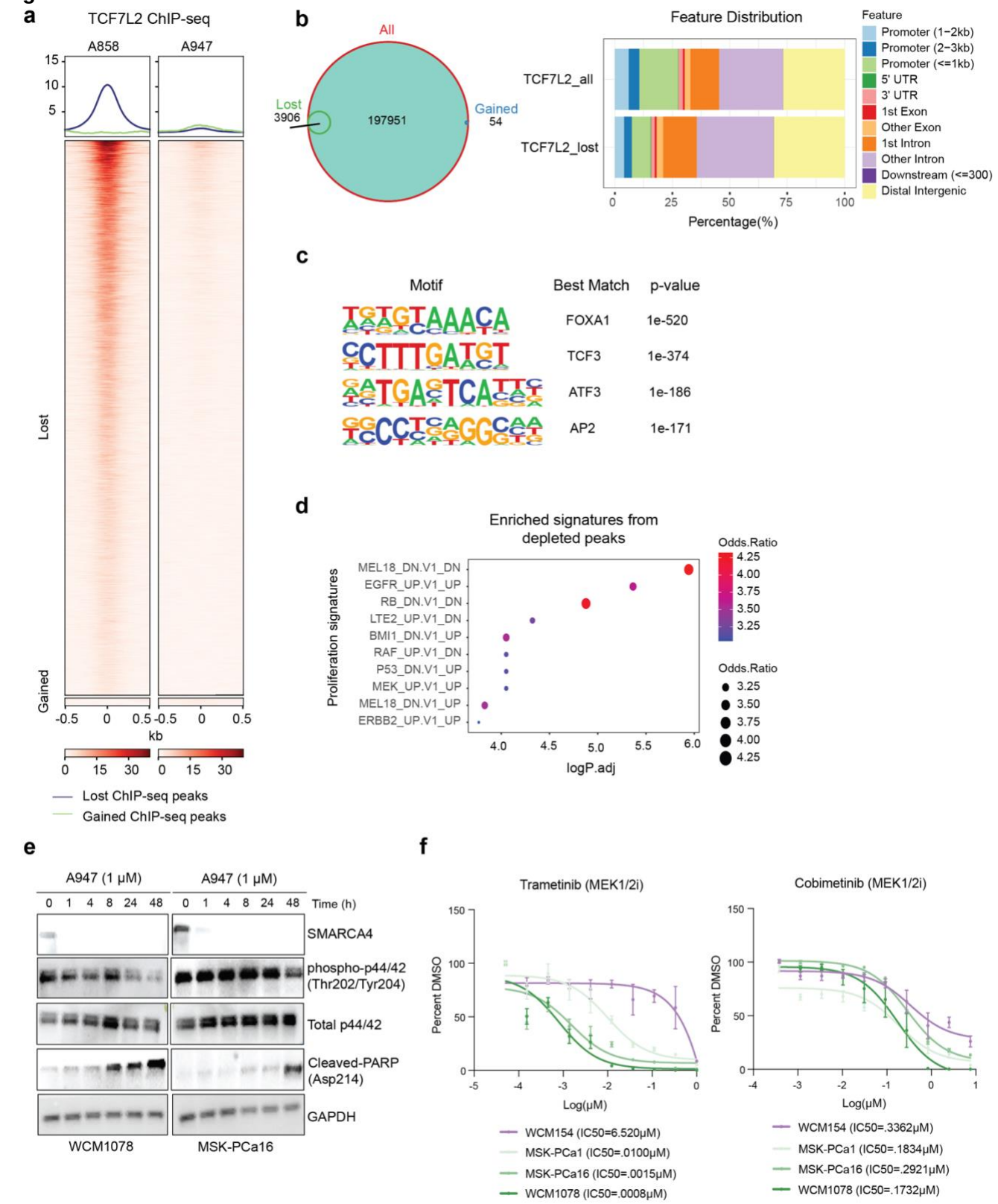
a
TCF7L2 ChIP-seq
A858
A947
Lost
Gained
kb
Lost ChIP-seq peaks
Gained ChIP-seq peaks
b
All
Lost
3906
197951
Gained
54
Feature Distribution
TCF7L2_all
TCF7L2_lost
Percentage(%)
Feature
Promoter (1−2kb)
Promoter (2−3kb)
Promoter (<=1kb)
5' UTR
3' UTR
1st Exon
Other Exon
1st Intron
Other Intron
Downstream (<=300)
Distal Intergenic
c
Motif
Best Match
p-value
FOXA1
1e-520
TCF3
1e-374
ATF3
1e-186
AP2
1e-171
d
Enriched signatures from depleted peaks
Proliferation signatures
MEL18_DN.V1_DN
EGFR_UP.V1_UP
RB_DN.V1_DN
LTE2_UP.V1_DN
BMI1_DN.V1_UP
RAF_UP.V1_DN
P53_DN.V1_UP
MEK_UP.V1_UP
MEL18_DN.V1_UP
ERBB2_UP.V1_UP
logP.adj
Odds.Ratio
e
A947 (1 μM)
Time (h)
SMARCA4
phospho-p44/42 (Thr202/Tyr204)
Total p44/42
Cleaved-PARP (Asp214)
GAPDH
WCM1078
MSK-PCa16
f
Trametinib (MEK1/2i)
Cobimetinib (MEK1/2i)
Percent DMSO
Log(μM)
WCM154 (IC50=6.520μM)
MSK-PCa1 (IC50=.0100μM)
MSK-PCa16 (IC50=.0015μM)
WCM1078 (IC50=.0008μM)
WCM154 (IC50=.3362μM)
MSK-PCa1 (IC50=.1834μM)
MSK-PCa16 (IC50=.2921μM)
WCM1078 (IC50=.1732μM)

Fig.4 TCF7L2 is evicted from the chromatin upon SMARCA2/4 depletion

a, ChIP-seq read-density tornado plots from WCM1078 organoids treated with 1μM A858 or 1μM A947 for 24h (n = 2 biological replicates). Venn diagram indicating lost and gained regions.

b, Venn diagram indicating lost and gained regions from ChIP-seq data.

c, Motifs enriched in depleted peaks from WCM1078 treated for 24h with 1μM A947 identified using HOMER from TCF7L2 ChIP-seq.

d, GSEA of TCF7L2 ChIP-seq identified depleted peaks upon A947-treatment.

e, Immunoblot of indicated proteins at an indicated time upon treatment with 1μM A947. GAPDH serves as loading control.

f, Dose-response curves with indicated drugs after measurement of proliferation with Celltiter Glo 2.0 after 7-day treatment (n=2 independent biological experiments).

Figure 5

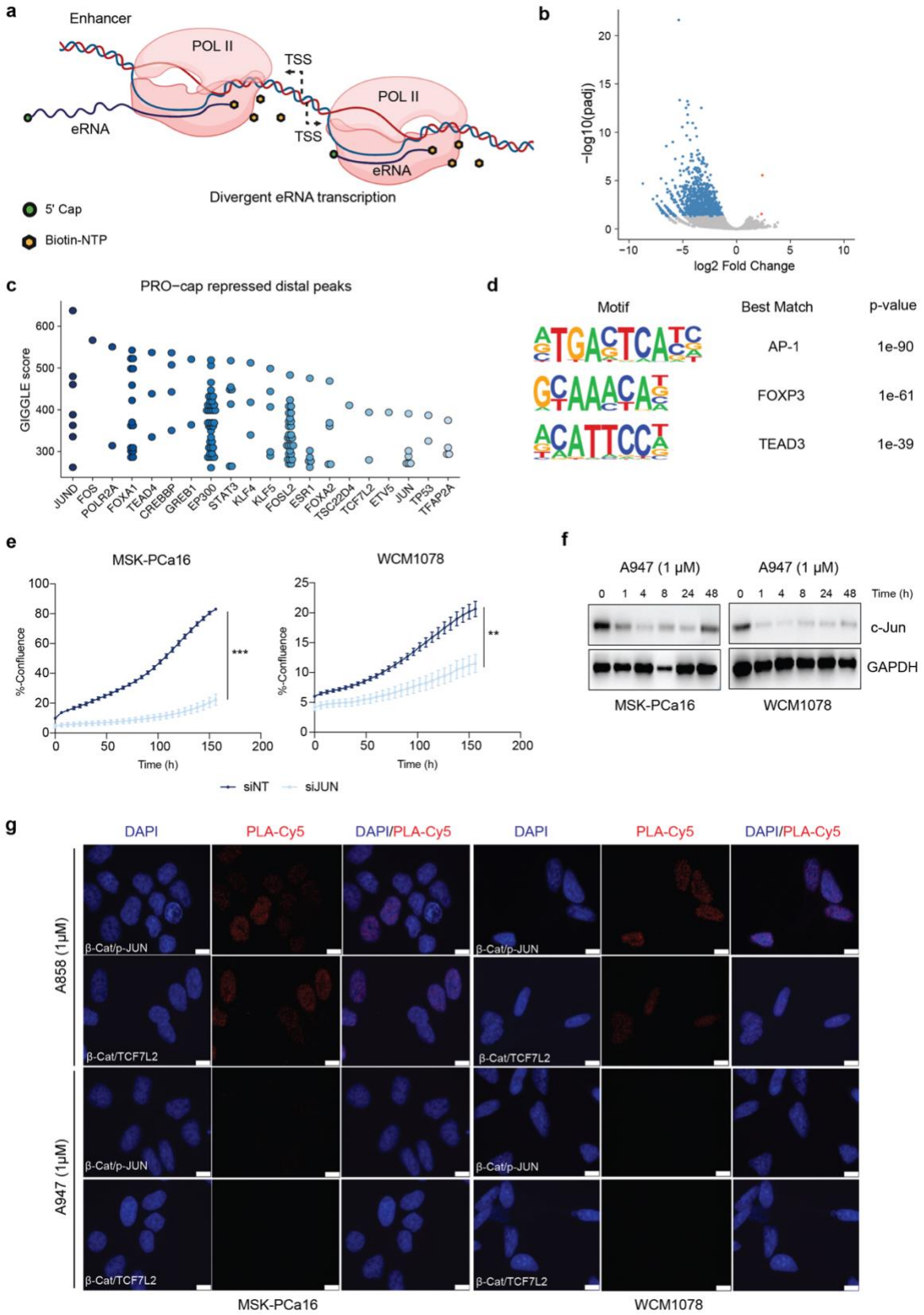
a
Enhancer
POL II
TSS
POL II
eRNA
TSS
eRNA
Divergent eRNA transcription
5' Cap
Biotin-NTP
b
−log10(padj)
log2 Fold Change
c
PRO−cap repressed distal peaks
GIGGLE score
JUND
FOS
POLR2A
FOXA1
TEAD4
CREBBP
GREB1
EP300
STAT3
KLF4
KLF5
FOSL2
ESR1
FOXA2
TSC22D4
TCF7L2
ETV5
JUN
TP53
TFAP2A
d
Motif
Best Match
p-value
AP-1
1e-90
FOXP3
1e-61
TEAD3
1e-39
e
MSK-PCa16
WCM1078
%-Confluence
Time (h)
siNT
siJUN
f
A947 (1 μM)
A947 (1 μM)
Time (h)
c-Jun
GAPDH
MSK-PCa16
WCM1078
g
DAPI
PLA-Cy5
DAPI/PLA-Cy5
A858 (1μM)
A947 (1μM)
β-Cat/p-JUN
β-Cat/TCF7L2
MSK-PCa16
WCM1078

Fig.5 AP-1 enhancer sites are modulated upon A947-treatment in CRPC-WNT

a, Model of PRO-cap 5' capping (green) and biotinylation (yellow) to enrich and detect enhancer RNAs (eRNA) that are divergently transcribed.

b, Volcano plot of depleted and enriched distal regions upon treatment with 1μM A947 (over 1μM A858) in WCM1078 treated for 24h as detected by PRO-cap.

c, GIGGLE score from depleted distal PRO-cap peaks.

d, Motifs enriched in depleted peaks from WCM1078 treated for 24h with 1μM A947 identified using HOMER from PRO-cap.

e, Confluence of indicated cell lines transduced with siNon-targeting (NT) or siJUN measured by live-cell imaging using Incucyte S3 ($N = 2$, independent experiments). Data are presented as mean values +/− SEM and analyzed using two-way ANOVA (*$p < 0.05$, **$p < 0.01$, ***$p < 0.001$, ****$p < 0.0001$).

f, Immunoblot of indicated proteins at an indicated time upon treatment with 1μM A947. GAPDH serves as loading control.

g, PLA with indicated antibodies after treatment with 1μM A858 or A947 for 24h. DAPI was used for nuclear staining. Scale bar: 10 μm.

Figure 6

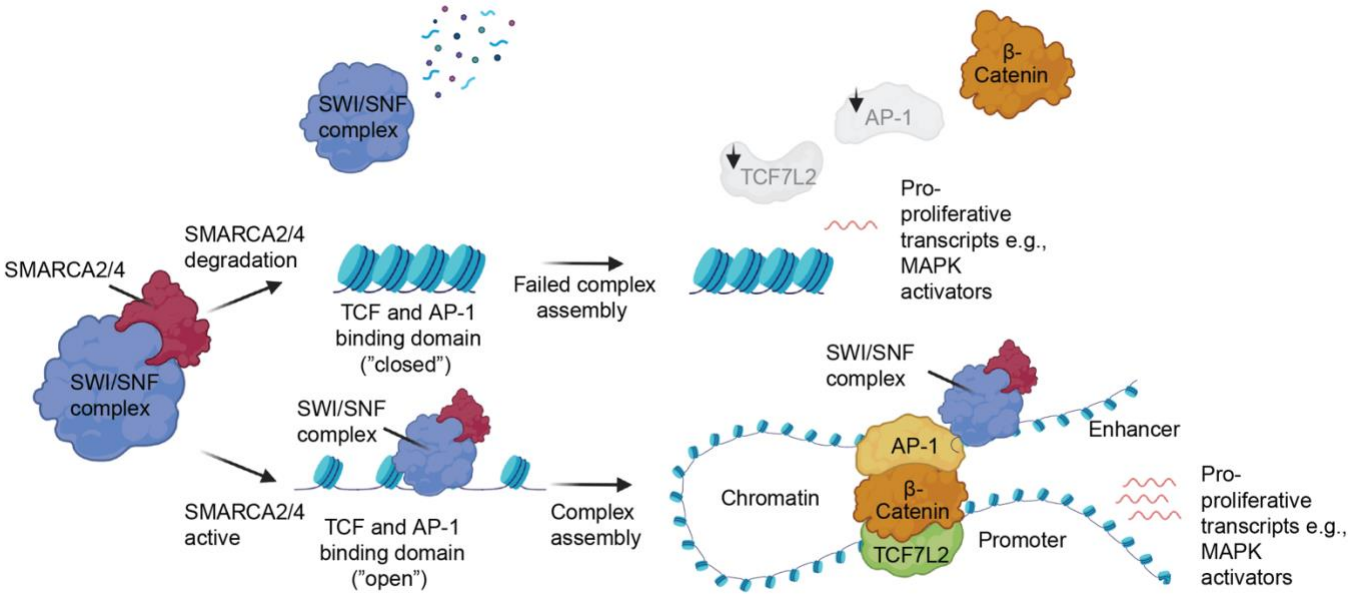

Fig.6 Working model of SWI/SNF complex function to maintain CRPC-WNT proliferation

Model of mechanism. SMARCA4-containing SWI/SNF complex maintains open chromatin confirmation of AP-1 and TCF binding domains, which leads to the assembly of a complex between AP-1 (e.g., c-Jun), TCF7L2 and β-Catenin. β-Catenin "bridges" the potential chromatin site interaction occupied by AP-1 TFs and TCF7L2 to positively regulate lineage-specific programs that orchestrate CRPC-WNT proliferation and survival. This complex cannot form when binding of the TFs to the chromatin is impaired by loss of SMARCA4. In addition, loss of SMARCA4 leads to downregulation of TCF7L2 and AP-1 (c-Jun) transcript and protein levels. Figure created with Biorender.com.

Supplementary Fig. 1

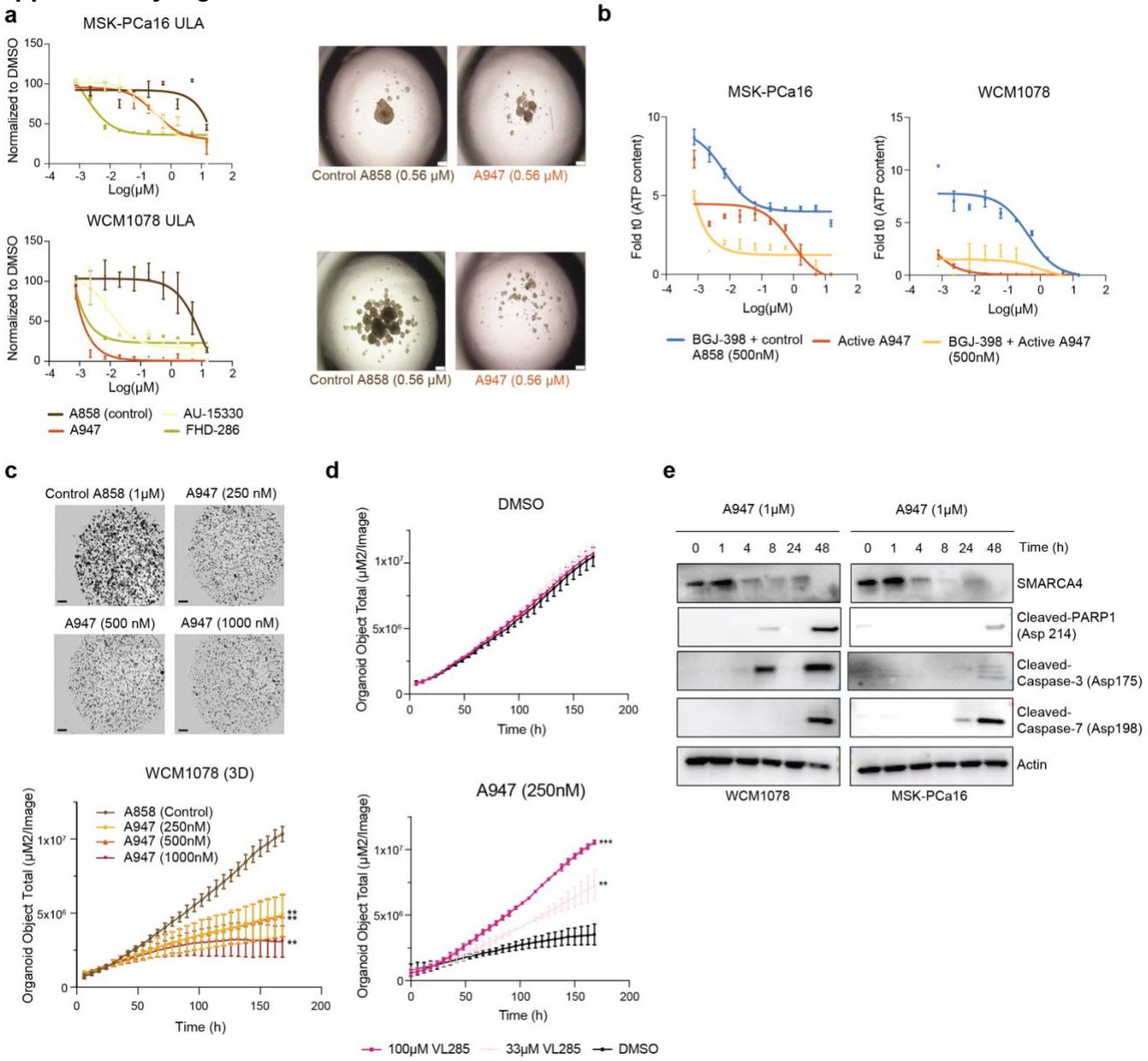

Supplementary Fig. 1. CRPC-WNT is a clinically relevant subtype that can be targeted by SMARCA2/4 PROTAC degraders

a, Proliferation measured with CellTiter Glo 2.0 at 7 days treated with dose response of indicated drugs. Brightfield microscopy pictures were taken 7 days after treatment. Scale bar: 100μm.

b, Proliferation measured with CellTiter Glo 3D at 7 days treated with dose response of indicated drugs.

c, Spheroid formation measured with Incucyte SX5 treated with indicated doses of A947 and 1μM A858. Brightfield microscopy pictures were taken at the endpoint. Scale bar: 800μm.

d, Spheroid formation measured with Incucyte SX5 treated with indicated doses of VL285 or DMSO combined with a dose of 250nM A947.

e, Immunoblot of indicated proteins in CRPC-WNT cell lines treated with A947 (1µM) for the indicated time. β-Actin serves as a loading control and is probed in a representative immunoblot.

Supplementary Fig. 2

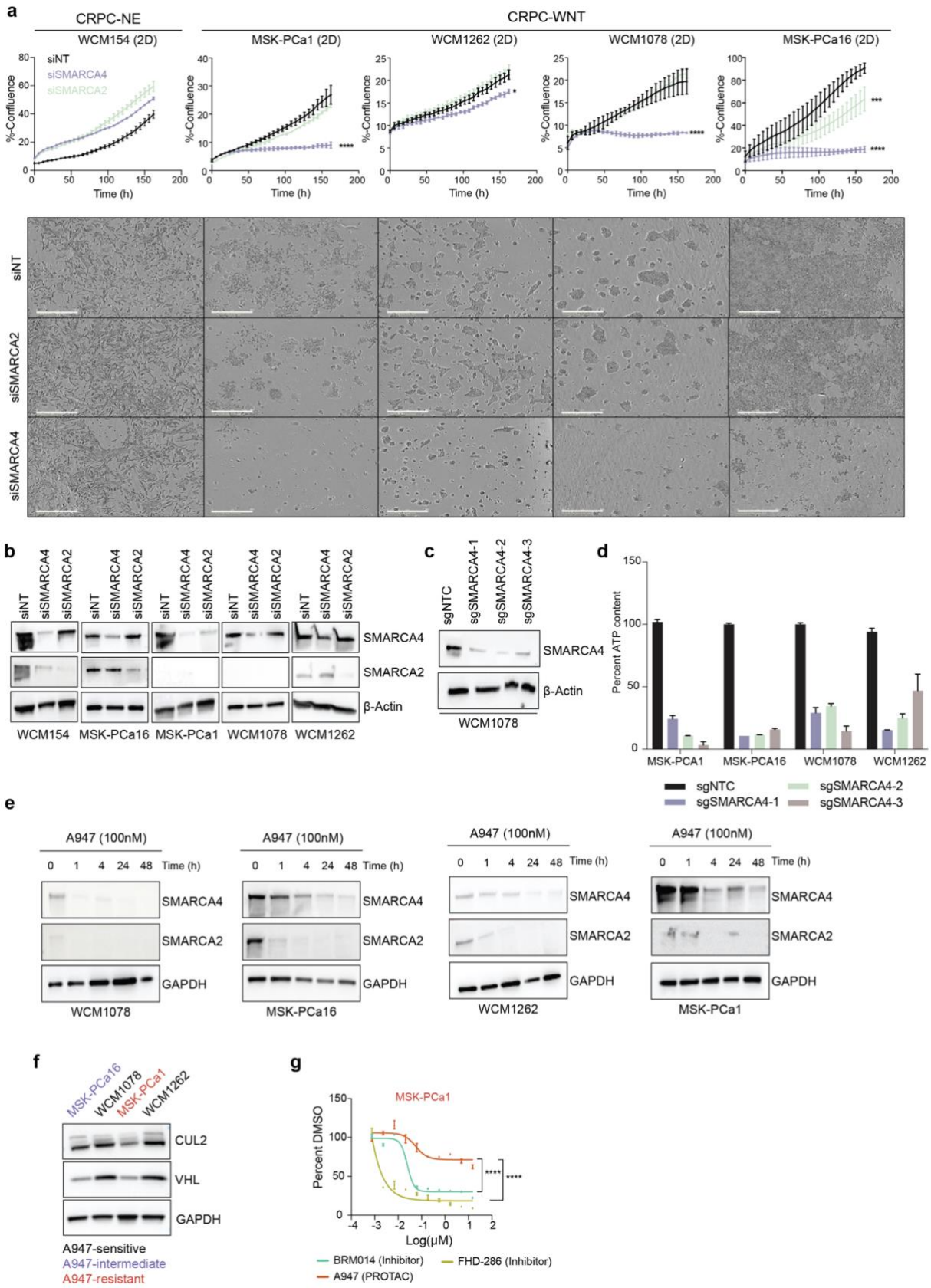

Supplementary Fig. 2. CRPC-WNT organoids are SMARCA4 but not SMARCA2 dependent

a, Confluence of indicated cell lines transduced with siNon-targeting (NT), siSMARCA2 or siSMARCA4 measured by live-cell imaging using Incucyte S3

(N = 3 independent experiments). Brightfield microscopy of indicated cell lines at Incucyte assay endpoint, Scale bars: 400µm. Data are presented as mean values +/− SEM and analyzed using two-way ANOVA (*$p < 0.05$, **$p < 0.01$, ***$p < 0.001$, ****$p < 0.0001$).

b, Immunoblot of indicated proteins in indicated cell lines transfected with respective siRNA after 72h. β-Actin represents loading control and is probed in a representative immunoblot.

c, Immunoblot of indicated proteins in WCM1078 transduced with respective sgRNA after 72h. β-Actin represents loading control and is probed in a representative immunoblot.

d, Proliferation was measured with CellTiter Glo 3D, and the indicated cell lines were transduced with sgRNAs against SMARCA4 after 10 days of growth (n = 3 independent biological experiments).

e, Immunoblot of indicated proteins in indicated cell lines treated with 100nM A947 for up to 48h. GAPDH serves as loading control.

f, Immunoblot of indicated proteins in indicated cell lines. GAPDH serves as a loading control and is probed in a representative immunoblot.

g, Proliferation measured of MSK-PCa1 treated with dose response of indicated drugs after 7 days of growth (N = 3 independent experiments). Data are presented as mean values +/− SEM and analyzed using two-way ANOVA (****$p < 0.0001$).

Supplementary Fig. 3

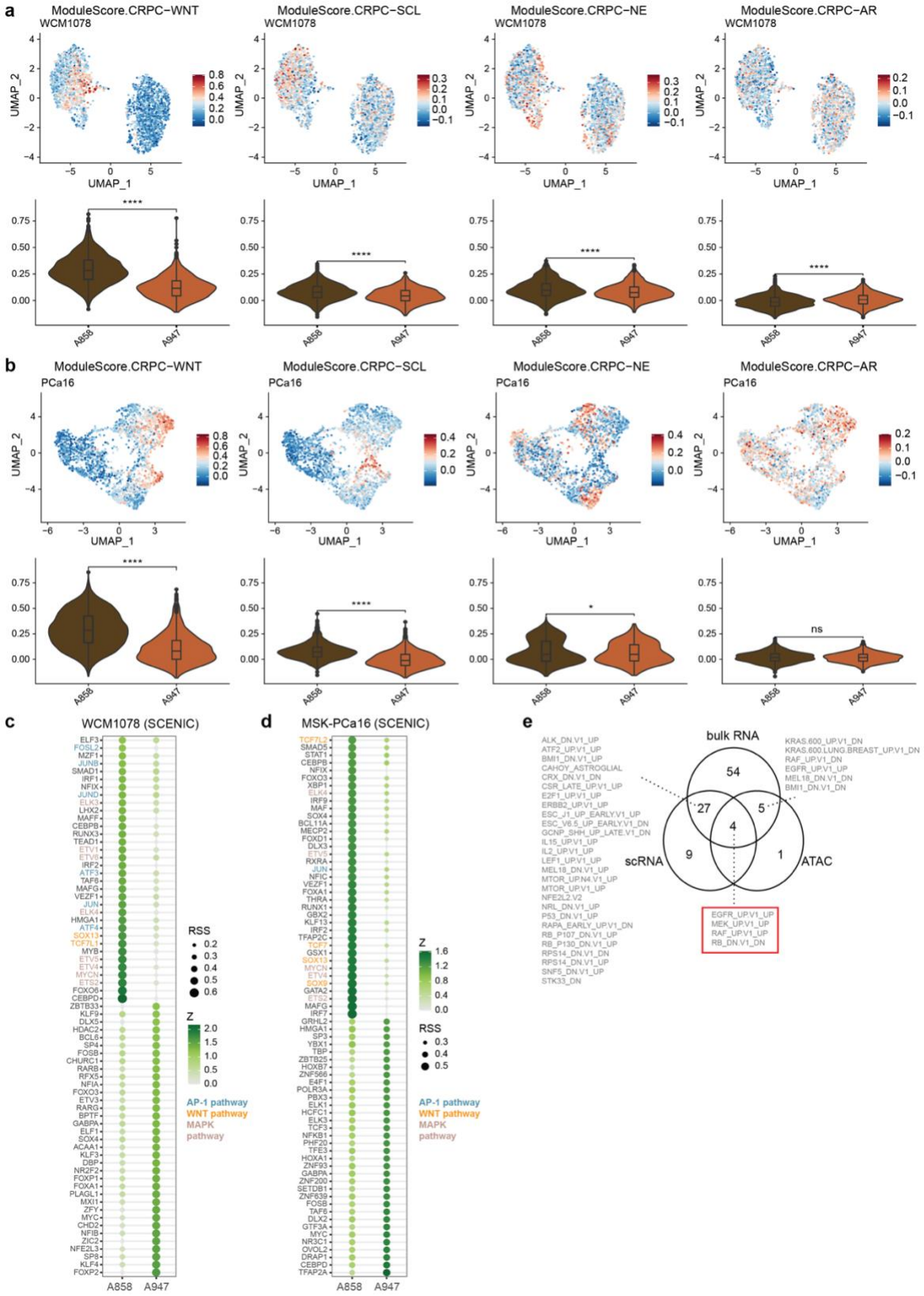

Supplementary Fig. 3. A947-treatment consistently modulates lineage-defining CRPC-WNT signature and master TFs

a, UMAP plot of indicated Tang et al.[35] scores in WCM1078 organoids treated with either 1µM A858 or 1µM A947 for 72h. Violin plots correspond to the UMAP plot above. Analyzed using the Wilcoxon test (****$p < 0.0001$).

b, UMAP plot of indicated Tang et al.[35] scores in MSK-PCa16 organoids treated with either 1µM A858 or 1µM A947 for 72h. Violin plots correspond to the UMAP plot above. Analyzed using Wilcoxon test (ns=not significant, *$p < 0.05$, **$p < 0.01$, ***$p < 0.001$, ****$p < 0.0001$).

c, Bubble plot of SCENIC results from WCM1078 organoids treated with either 1µM A858 or 1µM A947 for 72h.

d, Bubble plot of SCENIC results from MSK-PCa16 organoids treated with either 1µM A858 or 1µM A947 for 72h.

e, Venn diagram of intersect of C6:oncogenic signatures that are A947-treatment downregulated significantly between ATAC-seq, bulk RNA-seq, and scRNA-seq in WCM1078.

Supplementary Fig. 4

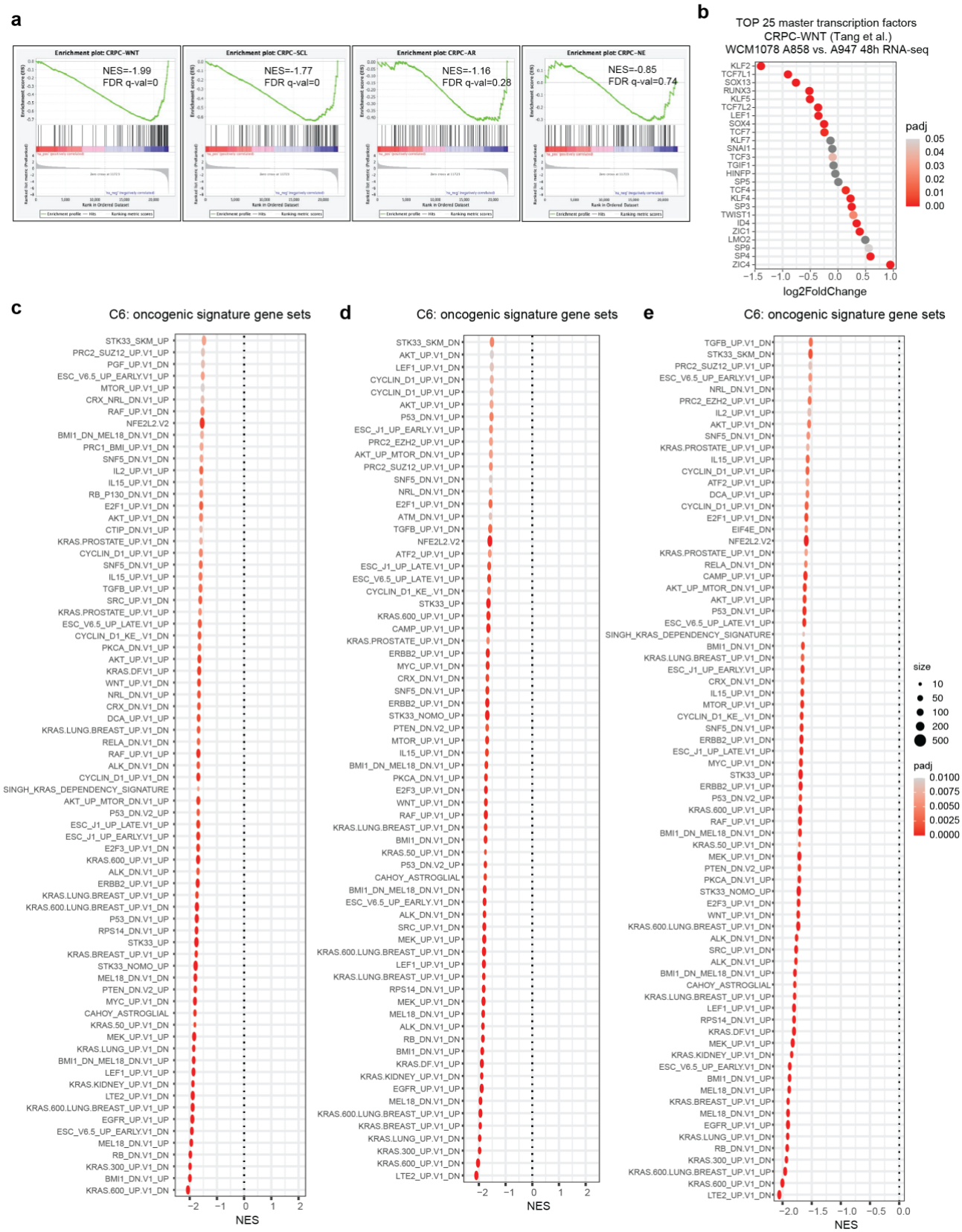

Supplementary Fig. 4. CRPC-WNT organoids become deregulated in multiple proliferative pathways upon SMARCA2/4 degradation

a, GSEA enrichment plots from WCM1078 treated with 1µM A947 for 48h RNA-seq data.

b, Dot plot of expression levels of top 25 most active CRPC-WNT master transcription (determined by Tang et al.) from 1µM A947-treated WCM1078 (48h) bulk RNA-seq data.

b, Bubble plot from C6 oncogenic gene setsWCM1078 treated with 1µM A947 for 24h RNA-seq data.

c, Bubble plot from C6 oncogenic gene sets WCM1078 treated with 1µM A947 for 48h RNA-seq data.

d, Bubble plot from C6 oncogenic gene sets WCM1078 treated with 1µM A947 overlap (24h and 48h) RNA-seq data.

Supplementary Fig. 5

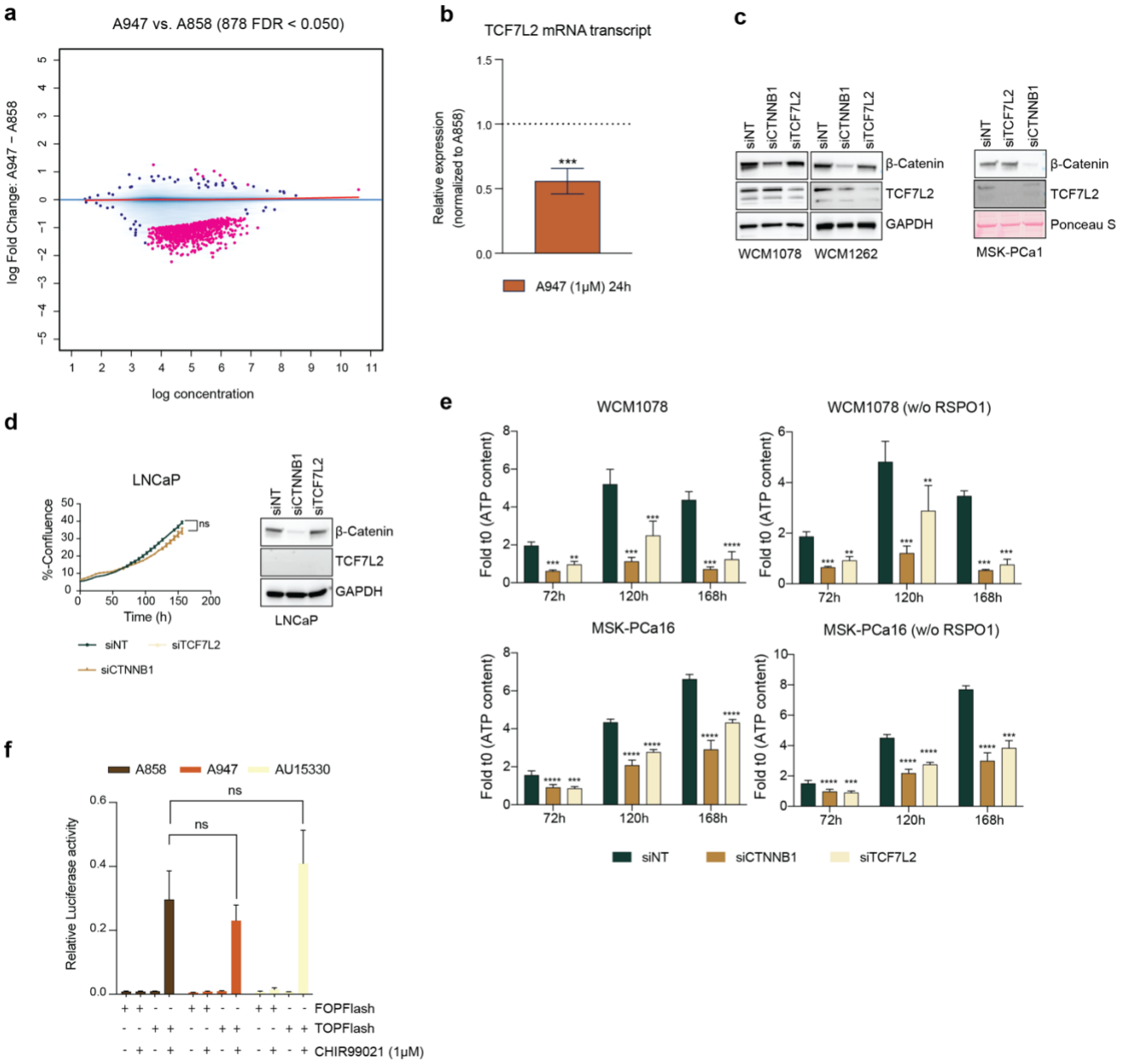

Supplementary Fig. 5. Dependency on TCF7L2 is CRPC-WNT specific

a, ATAC-seq differential accessibility plot from WCM1078 organoids treated for 24h with 1μM A947 or A858.

b, RT-PCR measurement of TCF7L2 mRNA in WCM1078 after treatment with indicated drugs. The housekeeping gene is GAPDH.

c, Immunoblot of indicated proteins 72h after transfection with indicated siRNA. GAPDH and Ponceau S serve as loading control.

d, Growth data measured by live-cell imaging (Incucyte S3) upon transfection of indicated siRNA. Data are presented as mean values +/− SEM and analyzed using two-way ANOVA (ns= not significant, *$p < 0.05$).

e, Proliferation was measured with CellTiter Glo 2.0 upon transfection of the indicated siRNA. Data are presented as mean values +/− SEM and analyzed using Students t-test (*$p < 0.05$, **$p < 0.01$, ***$p < 0.001$, ****$p < 0.0001$).

f The TOPFlash TCF/LEF reporter assay was measured after 48h upon transfection and 24h upon treatment with indicated drugs in HEK293T cells. FOPFlash serves as a negative control. Data are presented as mean values +/− SEM and analyzed using Students t-test (ns= not significant, *$p < 0.05$, **$p < 0.01$, ***$p < 0.001$).

Supplementary Fig. 6

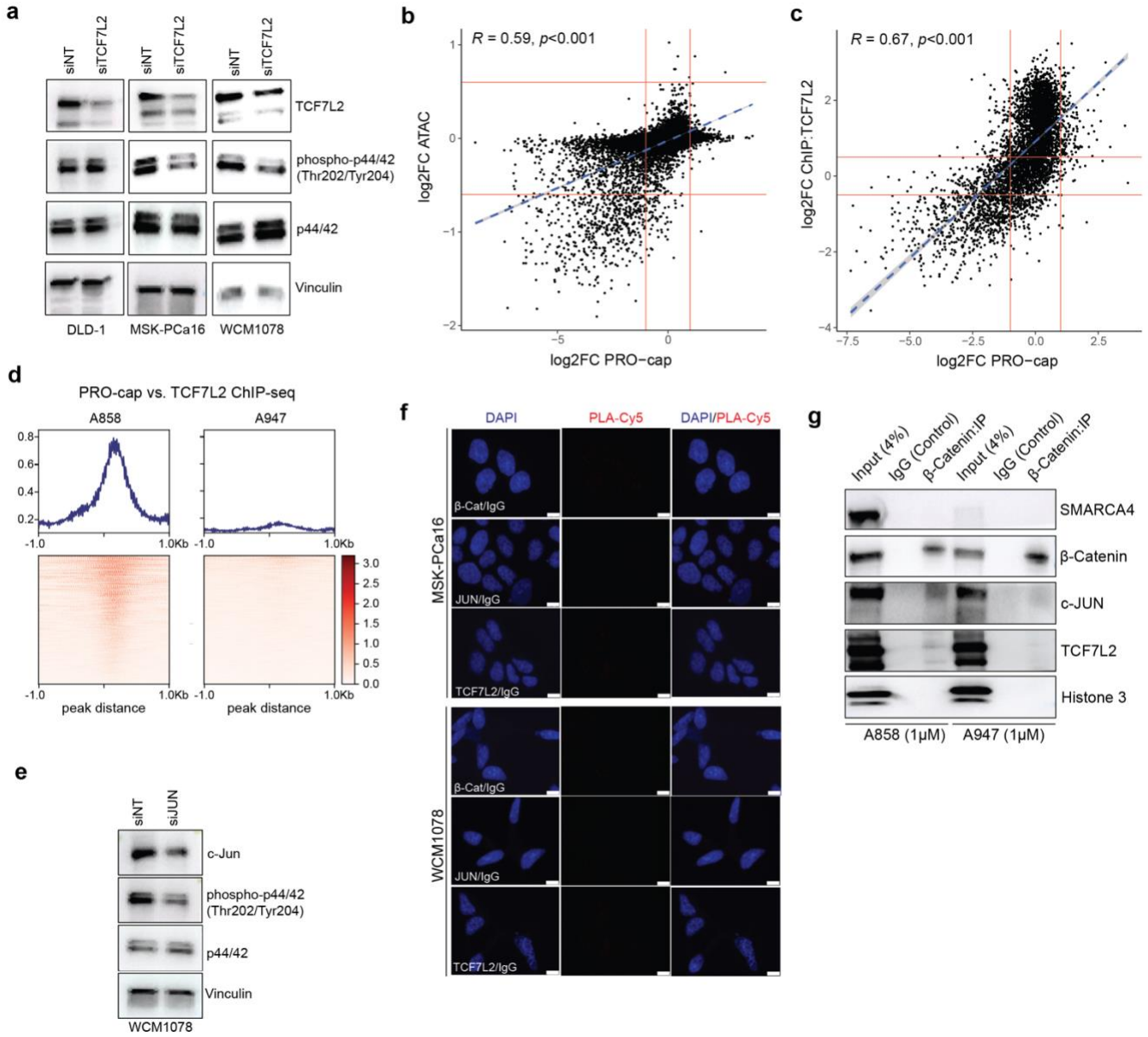

Supplementary Fig. 6. AP-1 and TCF7L2 modulate MAPK signaling in CRPC-WNT

a, Immunoblot of indicated proteins at indicated time upon transfection with siTCF7L2 after 72h. Vinculin serves as a loading control.

b, Correlation plot comparing ATAC-seq and PRO-cap from A947-treated WCM1078.

c, Correlation plot comparing TCF7L2 ChIP-seq and PRO-cap from A947-treated WCM1078.

d, Density tornado plot from overlap of TCF7L2 ChIP-seq and PRO-cap.

e, Immunoblot of indicated proteins at the indicated time upon transfection with siJUN after 72h. Actin serves as loading control.

f, PLA with indicated antibodies after treatment with 1μM A858 or A947 for 24h. DAPI was used for nuclear staining. Scale bar: 10 μm.

g, Immunoblot of indicated proteins after co-immunoprecipitation with β-Catenin antibody from MSK-PCa16 nuclear extracts after 24h treatment with 1μM control A858 or A947. Rabbit IgG serves as the isotype control, and Histone 3 (H3) serves as the control for nuclear extract.